THESIS FOR THE DEGREE OF LICENTIATE OF ENGINEERING

CTH-NT-341 February 2020

A neutron noise solver based on a discrete ordinates method

HUAIQIAN YI

CHALMERS
UNIVERSITY OF TECHNOLOGY

Division of Subatomic, High Energy and Plasma Physics
Department of Physics
CHALMERS UNIVERSITY OF TECHNOLOGY
Gothenburg, Sweden 2020

A neutron noise solver based on a discrete ordinates method

HUAIQIAN YI

Technical report no CTH-NT-341
Division of Subatomic, High Energy and Plasma Physics
Department of Physics
Chalmers University of Technology
SE-412 96 Gothenburg
Sweden
Telephone + 46 (0)31-772 1000

Chalmers Digital Print
Gothenburg, Sweden 2020

A neutron noise solver based on a discrete ordinates method

HUAIQIAN YI
Division of Subatomic, High Energy and Plasma Physics
Department of Physics
Chalmers University of Technology

Abstract

A neutron noise transport modelling tool is presented in this thesis. The simulator allows to determine the static solution of a critical system and the neutron noise induced by a prescribed perturbation of the critical system. The simulator is based on the neutron balance equations in the frequency domain and for two-dimensional systems. The discrete ordinates method is used for the angular discretization and the diamond finite difference method for the treatment of the spatial variable. The energy dependence is modelled with two neutron energy groups. The conventional inner-outer iterative scheme is employed for solving the discretized neutron transport equations. For the acceleration of the iterative scheme, the diffusion synthetic acceleration is implemented.

The convergence rate of the accelerated and unaccelerated versions of the simulator is studied for the case of a perturbed infinite homogeneous system. The theoretical behavior predicted by the Fourier convergence analysis agrees well with the numerical performance of the simulator. The diffusion synthetic acceleration decreases significantly the number of numerical iterations, but its convergence rate is still slow, especially for perturbations at low frequencies.

The simulator is further tested on neutron noise problems in more realistic, heterogeneous systems and compared with the diffusion-based solver. The diffusion synthetic acceleration leads to a reduction of the computational burden by a factor of 20. In addition, the simulator shows results that are consistent with the diffusion-based approximation. However, discrepancies are found because of the local effects of the neutron noise source and the strong variations of material properties in the system, which are expected to be better reproduced by a higher-order transport method such as the one used in the new solver.

Keywords: Neutron noise, nuclear reactor modelling, deterministic neutron transport methods, discrete ordinates, diffusion synthetic acceleration, convergence analysis

List of Publications

Papers included in the thesis:

PAPER I

H. Yi, P. Vinai and C. Demazière, "A discrete ordinates solver with diffusion synthetic acceleration for simulations of 2-D and 2-energy group neutron noise problems," *International Conference on Mathematics and Computational Methods applied to Nuclear Science and Engineering, M&C 2019*, Portland, Oregon USA, August 25-29, 2019.
https://doi.org/10.5281/zenodo.3567612

PAPER II

A. Mylonakis, H. Yi, P. Vinai and C. Demazière, "Neutron noise simulations in a heterogeneous system: A comparison between a diffusion-based and a discrete ordinates solver," *International Conference on Mathematics and Computational Methods applied to Nuclear Science and Engineering, M&C 2019*, Portland, Oregon USA, August 25-29, 2019.
https://doi.org/10.5281/zenodo.3567577

The author's contribution to the included papers:

PAPER I: Huaiqian Yi (HY) developed the transport neutron noise code, performed the theoretical and the simulation work for the convergence analysis of the solver, interpreted the results, and wrote the paper together with the co-authors.

PAPER II: HY developed the model for the discrete ordinates solver, performed the simulations with the discrete ordinates solver, prepared the plots about the comparison between the discrete ordinates solver and CORE SIM, contributed to the interpretation of the results.

Papers not related to the thesis subject and not included in the thesis:

H. Yi, C. Demazière, P. Vinai and J. Leppänen, "Development and Test of a Hybrid Probabilistic-Deterministic Framework Based on The Interface Current Method," *International Conference on Mathematics and Computational Methods applied to Nuclear Science and Engineering, M&C 2019*, Portland, Oregon USA, August 25-29, 2019.

Acknowledgements

First and foremost, I would like to thank my supervisor Assoc. Prof. Paolo Vinai for his guidance in my daily work and in the preparation this thesis. The works could not be accomplished and the thesis would not be close to its final state without his enormous help and support with great patience and dedication.

I would also like to thank my co-supervisor and examiner Prof. Christophe Demazière for insightful discussions and suggestions that helped to improve my work and the thesis.

Special thanks to Dr. Antonios Mylonakis for all the discussions we had in the office which helped me to overcome obstacles I encountered.

Lots of thanks to my family for their support and care throughout the whole time of my studies.

The research leading to these results has received funding from the Euratom research and training program 2014-2018 under grant agreement No. 754316. The financial support is gratefully appreciated.

Contents

Chapter 1 Introduction 1

1.1 Reactor neutron noise, and core monitoring and diagnostics 1

1.2 Structure of the thesis 2

Chapter 2 Multi-energy-group neutron noise equation 3

2.1 Neutron kinetics equations 3

2.2 Frequency domain transport neutron noise equation 5

Chapter 3 Neutron noise solver 7

3.1 Calculation scheme 7

3.2 Angular and spatial differencing schemes 8

3.2.1 Discrete ordinates method 8

3.2.2 Diamond finite difference scheme 9

3.3 Iterative scheme based on the transport sweep 11

3.4 Diffusion synthetic acceleration 14

Chapter 4 Verification of the neutron noise solver 19

4.1 Fourier convergence analysis of the dynamic module 19

4.1.1 Spectral radius for the unaccelerated scheme 19

4.1.2 Spectral radius of the DSA scheme 23

4.1.3 Convergence rate for 1-D and 2-D calculations 27

4.1.4 Convergence properties of the unaccelerated and DSA schemes 28

4.2 Neutron noise simulations in heterogeneous systems 30

4.3 Comparison with the diffusion-based simulator CORE SIM 34

4.3.1 Static flux and neutron noise calculated with the 2 solvers 34

4.3.2 Dependence on the frequency of the neutron noise source 35

Chapter 5 Conclusion and outlook 39

5.1 Summary 39

5.2 Outlook 40

References 41

Chapter 1

Introduction

The general background and the motivations of the work reported in this thesis are discussed together with the structure of the thesis.

1.1 Reactor neutron noise, and core monitoring and diagnostics

In nuclear reactors, the neutron flux is an important quantity to monitor, from an operational and safety viewpoint, since it is proportional to the reactor power output. Therefore, nuclear reactors are equipped with detectors for neutron flux measurements. The signals of these detectors show small fluctuations around the expected mean values, even under normal, steady state operating conditions. Such fluctuations are referred to as reactor neutron noise. In reactors operating at a high-power-level, this phenomenon is driven by perturbations such as vibrations of reactor components, disturbances in the operational conditions, etc. From the analysis of the neutron noise it is possible to obtain information about the dynamic properties of a reactor, identify anomalous patterns and, if necessary, take appropriate actions before dangerous situations arise [1, 2, 3].

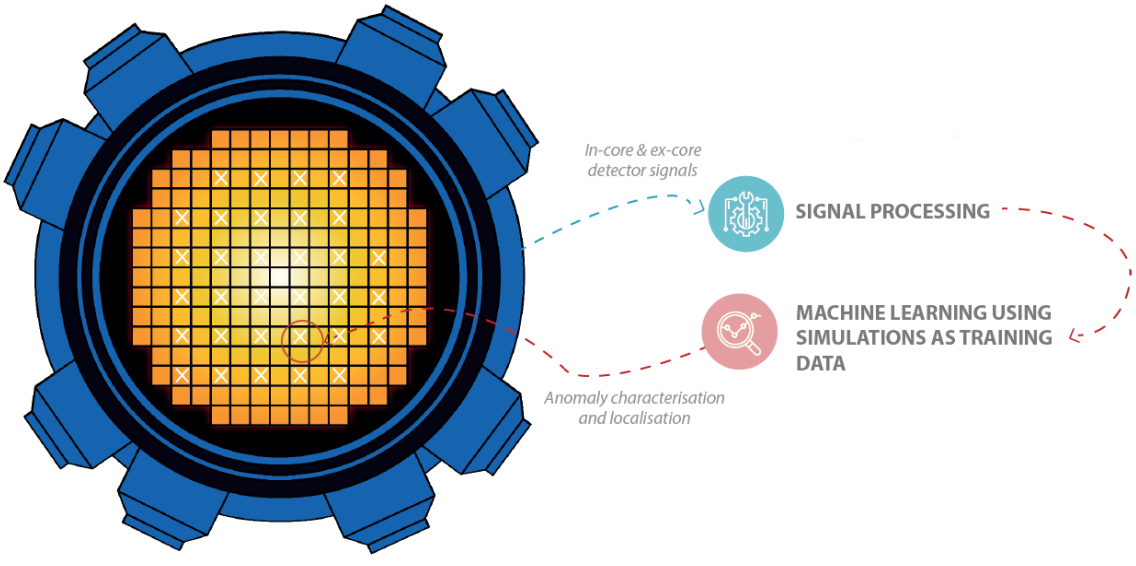

Figure 1.1 Illustration of using reactor neutron noise for core monitoring and diagnostics. [3]

The use of neutron noise analysis for core monitoring and diagnostics requires the modelling of the reactor transfer function. The function describes the response of the neutron flux in the core induced by any possible perturbation. Its inversion allows to identify and locate the noise source from the measured neutron noise. Given the complexity of a reactor system, this task cannot be performed in an analytical manner, so numerical methods must be used.

Most of the past work in the modelling of the transfer function relies on neutron diffusion theory, e.g. [4]. The advantage of this approach is that neutron noise problems in relatively large systems can be simulated without heavy computational efforts. Nevertheless, recent efforts also focus on higher-order deterministic [5] or stochastic [6, 7, 8] methods for solving the transport neutron noise equation. Although these methods are more computationally expensive, they can provide more detailed results and be used to assess the limitations of the diffusion approximation for neutron noise applications.

In the current thesis the first steps in the development of a higher-order transport solver for neutron noise simulations are presented. This research activity is part of the CORTEX project which aims to investigate reactor core monitoring and diagnostic techniques based on the analysis of neutron noise [2] and is supported by EU within the framework HORIZON 2020 – EURATOM.

1.2 Structure of the thesis

The thesis is built from the contents of Paper I and Paper II and is structured as follows. In Chapter 2, the multi-energy-group neutron noise equations in the frequency domain are derived. In Chapter 3, the numerical algorithms used to solve the neutron noise equation in the case of two-energy groups and two-dimensional geometry, are described. In Chapter 4, the analysis of the convergence of the solver and the comparison with a diffusion-based solution for a two-dimensional heterogeneous system with a localized neutron noise source are discussed. In Chapter 5, conclusions and an outlook for future work are provided.

Chapter 2

Multi-energy-group neutron noise equation

The time-dependent neutron balance equations used to describe nuclear reactor kinetics are introduced in Section 2.1. The transport neutron noise equation in the frequency domain is derived in Section 2.2. The solution of the neutron noise equations in the frequency domain is an advantageous strategy since it avoids expensive time-dependent simulations and requires only calculations for the frequency at which the neutron noise sources fluctuate.

2.1 Neutron kinetics equations

In a nuclear reactor, a fraction of the neutrons released from the fission reactions appears with a delay of seconds to minutes because of the beta decay of some fission products (the so-called precursors of delayed neutrons). Therefore, the modelling of the time-dependent behaviour of a reactor consists of a balance equation for the neutron density coupled to balance equations for the precursors of delayed neutrons. The precursors of delayed neutrons are usually grouped into a number of families according to their decay constants and a balance equation is given for each family. Then the neutron kinetics equations (with scattering treated as isotropic) reads, in a macroscopic sense, as:

$$\left[\frac{1}{v(\vec{r},E)}\frac{\partial}{\partial t}+\hat{\Omega}\cdot\nabla+\Sigma_t(\vec{r},E,t)\right]\psi(\vec{r},\hat{\Omega},E,t)$$
$$=\frac{1}{4\pi}\int\Sigma_s(\vec{r},E'\to E,t)\phi(\vec{r},E',t)dE'$$
$$+\frac{1}{4\pi k_{eff}}\left[\chi_p(\vec{r},E)\sum_q\left(1-\beta_q(\vec{r})\right)\int\nu\Sigma_f(\vec{r},E',t)\phi(\vec{r},E',t)dE'+\sum_q\chi_{d,q}(\vec{r},E)\lambda_q C_q(\vec{r},t)\right] \quad (2.1)$$

and

$$\frac{\partial C_q(\vec{r},t)}{\partial t}=\beta_q(\vec{r})\int\nu\Sigma_f(\vec{r},E',t)\phi(\vec{r},E',t)dE'-\lambda_q C_q(\vec{r},t), with\ q=1,\dots,Q \quad (2.2)$$

Eq. (2.1) is the balance equation for the neutrons and is written in terms of the angular flux $\psi(\vec{r},\hat{\Omega},E,t)$, which depends on the space vector $\vec{r}$, the angular direction $\hat{\Omega}$, the energy E and the time t. On the left-hand side, the three terms represent, respectively, the time variation of the neutron density, the streaming of neutrons and the disappearance of neutrons in the unit phase space. The right-hand side contains three source terms related to scattering, prompt and delayed neutrons emitted from fission reactions, respectively. For the scattering and prompt fission contributions, the scalar flux $\phi(\vec{r},E,t)$ estimated from the integration of the angular flux over all the angular directions, is used. In this equation, isotropy for the directions of the neutrons emitted from both prompt and delayed fission events are also assumed. The

contribution from the fission reactions is normalized using the effective multiplication factor k_{eff}, since in the current work only perturbations in critical systems are considered.

Eq. (2.2) gives the rate of change in the concentration $C_q(\vec{r},t)$ of the q-th family of delayed neutron precursors as the difference between the precursors created by fission and the precursors disappearing because of decay. This balance is equivalent to the balance of delayed neutrons since each precursor ultimately emits 1 delayed neutron.

In order to simplify the problem, the energy dependence is treated with the multi-group formalism. The range of all possible neutron energy is divided into *G* energy bins as:

$$[E_{min}: E_{max}] = \bigcup_{g=G}^{1} [E_g: E_{g-1}] \tag{2.3}$$

where the first group (g=1) has the neutrons with highest energies and the lowest energy neutrons belong to the last group ($g = G$). Eqs. (2.1) and (2.2) are integrated over the predefined energy bins and the following multi-group kinetics equations are obtained:

$$\left[\frac{1}{v_g(\vec{r})}\frac{\partial}{\partial t} + \hat{\Omega}\cdot\nabla + \Sigma_{t,g}(\vec{r},t)\right]\psi_g(\vec{r},\hat{\Omega},t)$$
$$= \frac{1}{4\pi}\sum_{g'}\Sigma_{s,g'\to g}(\vec{r},t)\phi_{g'}(\vec{r},t)$$
$$+\frac{1}{4\pi k_{eff}}\left[\chi_{p,g}(\vec{r})\sum_q\left(1-\beta_q(\vec{r})\right)\sum_{g'}\nu\Sigma_{f,g'}(\vec{r},t)\phi_{g'}(\vec{r},t) + \sum_q \chi_{d,q,g}(\vec{r})\lambda_q C_q(\vec{r},t)\right] \tag{2.4}$$

and

$$\frac{\partial C_q(\vec{r},t)}{\partial t} = \beta_q(\vec{r})\sum_{g'}\nu\Sigma_{f,g'}(\vec{r},t)\phi_{g'}(\vec{r},t) - \lambda_q C_q(\vec{r},t) \tag{2.5}$$

Setting the time derivatives in Eqs. (2.4) and (2.5) equal to zero, leads to the static equation:

$$\left[\hat{\Omega}\cdot\nabla + \Sigma_{t,g,0}(\vec{r})\right]\psi_{g,0}(\vec{r},\hat{\Omega}) = \frac{1}{4\pi}\sum_{g'}\Sigma_{s,g'\to g,0}(\vec{r})\phi_{g',0}(\vec{r})$$
$$+\frac{1}{4\pi k_{eff}}\left[\chi_{p,g}(\vec{r})\sum_q\left(1-\beta_q(\vec{r})\right) + \sum_q\chi_{d,q,g}(\vec{r})\beta_q(\vec{r})\right]\sum_{g'}\nu\Sigma_{f,g',0}(\vec{r})\phi_{g',0}(\vec{r}) \tag{2.6}$$

where the static quantities are denoted with the subscript "0". Eq. (2.6) corresponds to an eigenvalue problem whose solution gives both the eigenvalue k_{eff} and the static neutron fluxes.

2.2 Frequency domain transport neutron noise equation

The derivation of the transport neutron noise equation in the frequency domain follows a standard procedure used already in other works, e.g. [1, 4].

A critical system is assumed to be affected by a perturbation that can be described by a small, stationary fluctuation of the macroscopic neutron cross-sections around their mean values. The perturbation induces small fluctuations of the neutron flux and of the delayed neutron precursor concentrations. These quantities then can be written as the sum of a static mean value and a fluctuating part, such as:

$$X(\vec{r},t) = X_0(\vec{r}) + \delta X(\vec{r},t) \tag{2.7}$$

Eq. (2.7) is used for the macroscopic cross-sections, the delayed neutron precursor concentrations, the angular and the scalar neutron flux, into the neutron kinetics equations (2.4) and (2.5). The second order perturbation terms are neglected because the fluctuations are small and linear theory can be applied. The static equation (2.6) is subtracted and a temporal Fourier transform is performed. The resulting equation is the transport neutron noise equation in the frequency domain and reads as:

$$\left[\hat{\Omega}\cdot\nabla + \Sigma_{t,g,0}(\vec{r}) + \frac{i\omega}{v_g(\vec{r})}\right]\delta\psi_g(\vec{r},\hat{\Omega},\omega) = \frac{1}{4\pi}\sum_{g'}\Sigma_{s,g'\to g,0}(\vec{r})\delta\phi_{g'}(\vec{r},\omega)$$
$$+\frac{1}{4\pi k_{eff}}\left[\chi_{p,g}(\vec{r})\sum_q\left(1-\beta_q(\vec{r})\right)+\sum_q\chi_{d,q,g}(\vec{r})\frac{\lambda_q\beta_q(\vec{r})}{i\omega+\lambda_q}\right]\sum_{g'}\nu\Sigma_{f,g',0}(\vec{r})\delta\phi_{g'}(\vec{r},\omega)$$
$$+S_g(\vec{r},\hat{\Omega},\omega) \tag{2.8}$$

where the noise source $S_g(\vec{r},\hat{\Omega},\omega)$ has the following expression:

$$\mathrm{S_g}(\vec{r},\hat{\Omega},\omega) = -\delta\Sigma_{t,g}(\vec{r},\omega)\psi_{g,0}(\vec{r},\hat{\Omega}) + \frac{1}{4\pi}\sum_{g'}\delta\Sigma_{s,g'\to g}(\vec{r},\omega)\phi_{g',0}(\vec{r})$$
$$+\frac{1}{4\pi k_{eff}}\left[\chi_{p,g}(\vec{r})\sum_q\left(1-\beta_q(\vec{r})\right)+\sum_q\chi_{d,q,g}(\vec{r})\frac{\lambda_q\beta_q(\vec{r})}{i\omega+\lambda_q}\right]\sum_{g'}\nu\delta\Sigma_{f,g'}(\vec{r},\omega)\phi_{g',0}(\vec{r}) \tag{2.9}$$

In the neutron noise equations, i is the imaginary unit and $\omega = 2\pi f$ is the angular frequency of the perturbation. As can be seen in Eqs. (2.8) and (2.9), k_{eff} and the static neutron fluxes are needed; therefore Eq. (2.6) must be first solved. Eq. (2.8) represents a fixed source problem with the fixed k_{eff} obtained from the static problem. The solution to the noise problem provides the angular neutron noise $\delta\psi_g$ and the scalar neutron noise $\delta\phi_g$ as complex numbers. Combining the real and imaginary parts of these quantities, amplitude and phase of the angular and scalar neutron noise can be estimated.

Chapter 3

Neutron noise solver

The computational methods and algorithms applied to solve the neutron noise equation are presented. In Section 3.1, the overall calculation scheme of the solver is provided. In Section 3.2, the discrete ordinates method for the angular discretization and the diamond finite difference method for the spatial discretization are introduced. In Section 3.3, the transport sweeps and the iterative procedure for solving the multigroup transport equations are discussed. In Section 3.4, the diffusion synthetic acceleration method is described.

3.1 Calculation scheme

As shown in Section 2.2, the solution of the neutron noise equations in the frequency domain needs the value of k_{eff} and the static fluxes. Therefore, the solver that is under development in this project, consists of a static and a dynamic module (see Fig. 3.1). The static module first solves the eigenvalue problem represented by Eq. (2.6) so that the space dependent static angular and scalar fluxes and the effective multiplication factor k_{eff} are estimated. The dynamic module then solves Eq. (2.8), provided with the inputs from the static module and the position, amplitude and frequency of the fluctuating perturbation. The two modules are independent, so the first step in the calculation does not need to be repeated for problems with the same static configuration but different neutron noise sources.

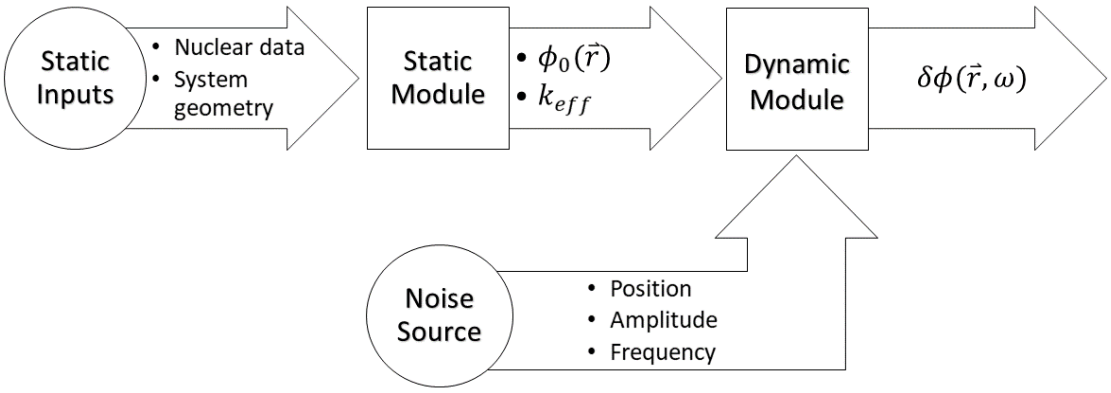

Figure 3.1 Overall calculation scheme of the discrete ordinates solver

3.2 Angular and spatial differencing schemes

When solving numerically the problem, the equations are discretized with respect to the independent variables. The energy discretization is discussed in Section 2.1 and leads to the multi-energy-group equations. In addition, the discrete ordinates method and the diamond finite difference method are used for the angular variable $\widehat{\Omega}$ and the spatial variable $\vec{r}$, respectively. Consistently with the neutron noise solver presented in this thesis, the discussions are hereinafter based on two-dimensional cases.

3.2.1 Discrete ordinates method

In this work, a discrete ordinate method is applied to the angular discretization of Eqs. (2.6) and (2.8). The discrete ordinates (S_N) method has been widely used in the nuclear community for solving the neutron transport equation because it is acknowledged for its simplicity in the derivation process, and for its good computational efficiency while avoiding excessive computer memory consumption [9].

The angular variable $\hat{\Omega}$ is expressed by the direction cosines. In the 2-D case, it is then given as:

$$\hat{\Omega} = \hat{\Omega}\left(\hat{\Omega}_x, \hat{\Omega}_y\right) = \hat{\Omega}\left(\hat{\Omega}\cdot\hat{e}_x, \hat{\Omega}\cdot\hat{e}_y\right) = \hat{\Omega}(\mu,\eta) \tag{3.1}$$

where $\hat{e}_x$ and $\hat{e}_y$ are the unit vectors in the positive direction of the two axes of the cartesian coordinate system. In the S_N method, the transport equations are evaluated along a fixed number of discrete angular directions.

Similar to the static case, the transport neutron noise equation for the generic discrete angular direction $\hat{\Omega}_n = \hat{\Omega}(\mu_n, \eta_n)$ can thus be written as:

$$\left[\mu_n\frac{\partial}{\partial x} + \eta_n\frac{\partial}{\partial y} + \Sigma_{t,g,0}(\vec{r}) + \frac{i\omega}{v_g(\vec{r})}\right]\delta\psi_{g,n}(\vec{r},\omega) = \frac{1}{2\pi}\sum_{g'}\Sigma_{s,g'\to g,0}(\vec{r})\delta\phi_{g'}(\vec{r},\omega)$$
$$+\frac{1}{2\pi k_{eff}}\left[\chi_{p,g}(\vec{r})\sum_q\left(1-\beta_q(\vec{r})\right) + \sum_q\chi_{d,q,g}(\vec{r})\frac{\lambda_q\beta_q(\vec{r})}{i\omega+\lambda_q}\right]\sum_{g'}\nu\Sigma_{f,g',0}(\vec{r})\delta\phi_{g'}(\vec{r},\omega)$$
$$+S_{g,n}(\vec{r},\omega) \tag{3.2}$$

with the noise source given as:

$$S_{g,n}(\vec{r},\omega) = -\delta\Sigma_{t,g}(\vec{r},\omega)\psi_{g,n,0}(\vec{r}) + \frac{1}{2\pi}\sum_{g'}\delta\Sigma_{s,g'\to g}(\vec{r},\omega)\phi_{g',0}(\vec{r})$$
$$+\frac{1}{2\pi k_{eff}}\left[\chi_{p,g}(\vec{r})\sum_q\left(1-\beta_q(\vec{r})\right) + \sum_q\chi_{d,q,g}(\vec{r})\frac{\lambda_q\beta_q(\vec{r})}{i\omega+\lambda_q}\right]\sum_{g'}\nu\delta\Sigma_{f,g'}(\vec{r},\omega)\phi_{g',0}(\vec{r}) \tag{3.3}$$

In Eq. (3.2) the notation $\delta\psi_{g,n}(\vec{r},\omega) = \delta\psi_g\left(\vec{r},\hat{\Omega}_n,\omega\right)$ is used to represent the angular neutron noise for the n-th discrete angular direction. The scalar neutron noise is calculated with a quadrature formula that approximates the angle integration:

$$\delta\phi_g(\vec{r},\omega) = \frac{\pi}{2}\sum_{n=1}^{N_0} w_n \delta\psi_{g,n}(\vec{r},\omega) \tag{3.4}$$

The parameter N_0 is the total number of discrete angular directions and the weights w_n are normalized according to the following relationship:

$$\sum_{n=1}^{N_0} w_n = 4 \tag{3.5}$$

The direction cosines and their corresponding weights can be determined with different quadrature sets. The widely applied level symmetric quadrature set (LQ_N) is chosen in this work. Using the LQ_N sets in two-dimensional geometry, the discrete ordinates approximation of order N has $(N+2)N/2$ discrete directions. The details of the level symmetric method can be found, e.g., in [9].

One major drawback of the S_N method applied to static calculations is the so called "ray effects". Unphysical results may be generated if a low order S_N approximation is used to solve problems defined in a highly absorbent media with localized source. This effect is also observed in the neutron noise problems that are discussed in Chapter 4. In this work, the most straightforward remedy, where the number of discrete ordinates is increased, is tested and it is shown to improve the results.

3.2.2 Diamond finite difference scheme

The discretization of the spatial variable is based on the diamond finite difference scheme. The method has been largely applied to the static equations [9]. Then the discussion is focused on the neutron noise equations.

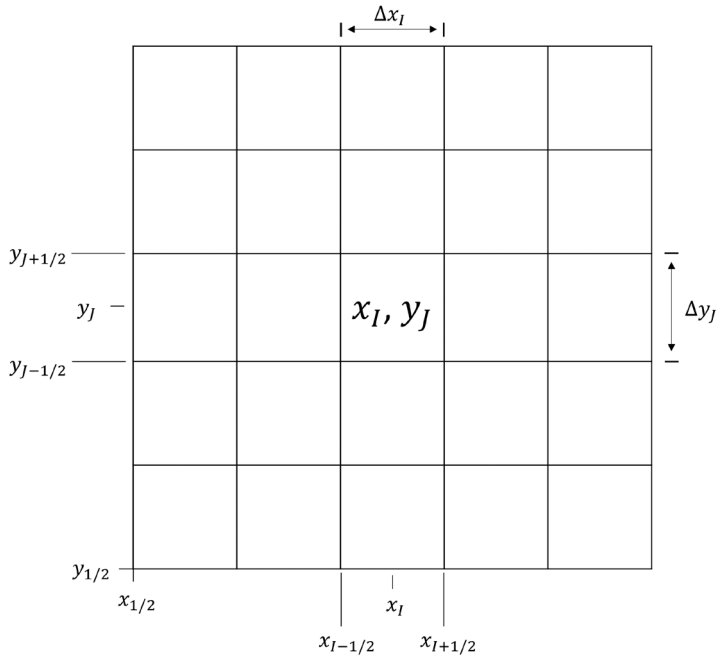

Figure 3.2 Two-dimensional domain with rectangular spatial mesh

A 2-dimensional domain is considered in the $x-y$ plane. As shown in Figure 3.2, the domain is divided into cells bounded by the coordinates $x_{1/2}, x_{3/2}, \cdots, x_{I_{max}+/2}$ in the direction x and $y_{1/2}, y_{3/2}, \cdots, y_{J_{max}+/2}$ in the direction y. Each cell thus are rectangles with width $\Delta x_I = x_{I+1/2} - x_{I-1/2}$ and $\Delta y_J = y_{J+1/2} - y_{J-1/2}$. In each cell, the system parameters take constant values and change only at the boundaries of the cells denoted by the half-integers. By integrating Eq. (3.2) over the generic cell $(I,\ J)$, the following relationship is obtained:

$$\frac{\mu_n}{\Delta x_I}\left[\delta\psi_{g,n,I+1/2,J}(\omega) - \delta\psi_{g,n,I-1/2,J}(\omega)\right] + \frac{\eta_n}{\Delta y_J}\left[\delta\psi_{g,n,I,J+1/2}(\omega) - \delta\psi_{g,n,I,J-1/2}(\omega)\right]$$
$$+\left[\Sigma_{t,g,0,I,J} + \frac{i\omega}{v_{g,I,J}}\right]\delta\psi_{g,n,I,J}(\omega) = \frac{1}{2\pi}\sum_{g'}\Sigma_{s,g'\to g,0,I,J}\delta\phi_{g',I,J}(\omega)$$
$$+\frac{1}{2\pi k_{eff}}\left[\chi_{p,g,I,J}\sum_{\mathrm{q}}\left(1-\beta_{q,I,J}\right) + \sum_{\mathrm{q}}\chi_{d,q,g,I,J}\frac{\lambda_q\beta_{q,I,J}}{i\omega+\lambda_q}\right]\sum_{g'}\nu\Sigma_{f,g',0,I,J}\delta\phi_{g',I,J}(\omega)$$
$$+S_{g,n,I,J}(\omega) \tag{3.6}$$

The neutron noise source term is equal to:

$$S_{g,n,I,J}(\omega) = -\delta\Sigma_{t,g,\mathrm{I,J}}(\omega)\psi_{g,n,0,\mathrm{I,J}} + \frac{1}{2\pi}\sum_{g'}\delta\Sigma_{s,g'\to g,\mathrm{I,J}}(\omega)\phi_{g',0,\mathrm{I,J}}$$
$$+\frac{1}{2\pi k_{eff}}\left[\chi_{p,g,I,J}\sum_{q}\left(1-\beta_{q,I,J}\right) + \sum_{\mathrm{q}}\chi_{d,q,g,I,J}\frac{\lambda_q\beta_{q,I,J}}{i\omega+\lambda_q}\right]\sum_{g'}\nu\delta\Sigma_{f,g',I,J}(\omega)\phi_{g',0,I,J} \tag{3.7}$$

In Eqs. (3.6) and (3.7) the edge averaged angular neutron noise values are defined as:

$$\delta\psi_{g,n,I\pm\frac{1}{2},J} = \frac{1}{\Delta \mathrm{y_J}}\int_{\Delta y_{J-\frac{1}{2}}}^{\Delta y_{J+\frac{1}{2}}}\delta\psi_{g,n}\left(x_{I\pm\frac{1}{2}}, y\right)dy \tag{3.8}$$

$$\delta\psi_{g,n,I,J\pm\frac{1}{2}} = \frac{1}{\Delta \mathrm{x_I}}\int_{\Delta x_{I-\frac{1}{2}}}^{\Delta x_{I+\frac{1}{2}}}\delta\psi_{g,n}\left(x, y_{J\pm\frac{1}{2}}\right)dx \tag{3.9}$$

and the cell averaged angular neutron noise is defined as:

$$\delta\psi_{g,n,I,J} = \frac{1}{\Delta \mathrm{y_J}\Delta \mathrm{x_I}}\int_{\Delta \mathrm{y}_{\mathrm{J}-\frac{1}{2}}}^{\Delta \mathrm{y}_{\mathrm{J}+\frac{1}{2}}}\int_{\Delta \mathrm{x}_{\mathrm{I}-\frac{1}{2}}}^{\Delta \mathrm{x}_{\mathrm{I}+\frac{1}{2}}}\delta\psi_{g,n}(x,y)dxdy \tag{3.10}$$

To relate the cell averaged angular neutron noise values to the edge averaged values, two auxiliary diamond difference approximations are required, such as:

$$\delta\psi_{g,n,I,J} = \frac{1}{2}\left(\delta\psi_{g,n,I+\frac{1}{2},J} + \delta\psi_{g,n,I-\frac{1}{2},J}\right) \tag{3.11}$$

$$\delta\psi_{g,n,I,J} = \frac{1}{2}\left(\delta\psi_{g,n,I,J+\frac{1}{2}} + \delta\psi_{g,n,I,J-\frac{1}{2}}\right) \tag{3.12}$$

The mesh for the dynamic module is the same as the mesh for the static module, so that the neutron noise source can be constructed using directly the fluxes and the correct k_{eff} from the criticality calculation.

Vacuum and reflective boundary conditions are implemented for the fully discretized transport equations. For vacuum boundary conditions, the boundary angular flux with directions pointing into the system is set to zero. For reflective boundary conditions, since the angle quadrature set is defined such that the directions are symmetric with respect to the origin, the entering boundary flux is set equal to the corresponding outgoing boundary flux.

The diamond difference method is an advantageous scheme because of the simplicity in its implementation. However, for static calculations, the method may cause negative surface fluxes, which are unphysical. This usually happens in systems with strong absorbing material while the computational mesh is not sufficiently fine. In the static module, the negative flux fixup algorithm is included: if negative fluxes are calculated, they are set to zero and the discretized transport equation is re-evaluated with zero exiting flux(es). For the dynamic module the issue of negative fluxes has not been encountered so far, since the calculations are performed in the frequency domain and the estimated neutron noise is a complex quantity.

3.3 Iterative scheme based on the transport sweep

The discussion is restricted to the case of two energy-groups, where the first group is the fast one, the second group is the thermal one, and up-scattering from the thermal to the fast group is neglected. The multi-energy-group case is planned to be investigated in the future of this research (see Chapter 5).

Both the static and dynamic modules rely on the conventional inner-outer iterative scheme for solving the multigroup discrete ordinates problem.

In the inner part of the iterative scheme, the spatial distribution of the neutron fluxes is solved using the conventional transport sweep algorithm. For the sweep procedure in the dynamic calculation, the g-th energy group and a direction that lies in the quadrant of the 2-D plane with $\mu_n > 0$ and $\eta_n > 0$, is considered. For the cell (I, J), the following equation is derived from Eq. (3.6):

$$\frac{\mu_n}{\Delta x}\left[\overline{\delta\psi}^{(\mathrm{l,m+1/2})}_{n,I+1/2,J}(\omega) - \overline{\delta\psi}^{(\mathrm{l,m+1/2})}_{n,I-1/2,J}(\omega)\right] + \frac{\eta_n}{\Delta y}\left[\overline{\delta\psi}^{(\mathrm{l,m+1/2})}_{n,I,J+1/2}(\omega) - \overline{\delta\psi}^{(\mathrm{l,m+1/2})}_{n,I,J-1/2}(\omega)\right]$$

$$+\overline{\overline{\Sigma^{\mathrm{dyn}}_{\mathrm{t},I,J}}}\,\overline{\delta\psi}^{(l,m+1/2)}_{n,I,J}(\omega)$$

$$= \frac{1}{2\pi}\overline{\overline{\Sigma_{ss}}}_{I,J}\,\overline{\delta\phi}^{(l,m)}_{I,J}(\omega) + \frac{1}{2\pi}\overline{\overline{\Sigma_{sd}}}_{I,J}\,\overline{\delta\phi}^{(l,M)}_{I,J}(\omega) + \frac{1}{2\pi}\bar{\bar{\chi}}_{\mathrm{I,J}}\,\overline{\overline{\nu\Sigma_{\mathrm{f}}}}^{T}_{I,J}\,\overline{\delta\phi}^{(l,0)}_{I,J}(\omega) + \bar{S}_{n,I,J}(\omega) \quad (3.13)$$

In the equation above, column-vectors and matrices are defined as:

$$\overline{\delta\psi}_{n,I,J}^{(l,m+1/2)} = \begin{bmatrix} \delta\psi_{1,n,I,J}^{(l,m+1/2)} \\ \delta\psi_{2,n,I,J}^{(l,m+1/2)} \end{bmatrix} \tag{3.14}$$

$$\overline{\delta\phi}_{I,J}^{(l,m)} = \begin{bmatrix} \delta\phi_{1,I,J}^{(l,m)} \\ \delta\phi_{2,I,J}^{(l,m)} \end{bmatrix} \tag{3.15}$$

$$\bar{S}_{i,j}(\omega) = \begin{bmatrix} S_{1,n,I,J}(\omega) \\ S_{2,n,I,J}(\omega) \end{bmatrix} \tag{3.16}$$

$$\overline{\overline{\Sigma_{ss}}}_{I,J} = \begin{bmatrix} \Sigma_{s,1\to1,0,I,J} & 0 \\ 0 & \Sigma_{s,2\to2,0,I,J} \end{bmatrix} \tag{3.17}$$

$$\overline{\overline{\Sigma_{sd}}}_{I,J} = \begin{bmatrix} 0 & \Sigma_{s,1\to2,0,I,J} \\ 0 & 0 \end{bmatrix} \tag{3.18}$$

$$\overline{\overline{\Sigma_{\mathrm{t},I,J}^{\mathrm{dyn}}}} = \begin{bmatrix} \Sigma_{t,1,0,I,J} + \dfrac{i\omega}{v_{1,I,J}} & 0 \\ 0 & \Sigma_{t,2,0,I,J} + \dfrac{i\omega}{v_{2,I,J}} \end{bmatrix} \tag{3.19}$$

$$\overline{\nu\Sigma_f}_{I,J} = \frac{1}{k_{eff}} [\nu\Sigma_{f,1,0,I,J} \quad \nu\Sigma_{f,2,0,I,J}]^T \tag{3.20}$$

$$\bar{\chi}_{I,J} = \begin{bmatrix} \chi_{\mathrm{p},1,I,J} \sum_{\mathrm{q}} (1 - \beta_{\mathrm{q},I,J}) + \sum_{\mathrm{q}} \chi_{\mathrm{d,q},1,I,J} \dfrac{\lambda_{\mathrm{q}} \beta_{\mathrm{q},I,J}}{i\omega + \lambda_{\mathrm{q}}} \\ \chi_{\mathrm{p},2,I,J} \sum_{\mathrm{q}} (1 - \beta_{\mathrm{q},I,J}) + \sum_{\mathrm{q}} \chi_{\mathrm{d,q},2,I,J} \dfrac{\lambda_{\mathrm{q}} \beta_{\mathrm{q},I,J}}{i\omega + \lambda_{\mathrm{q}}} \end{bmatrix} \tag{3.21}$$

Eq. (3.13) is written for the sweep performed at the $(m+1)$-th inner iteration within the $(l+1)$-th outer iteration. The index $(m+1/2)$ denotes evaluations of quantities before the updates made at the end of the $(m+1)$-th inner iteration. The right-hand side of Eq. (3.13) contains four source terms. The first term that represents the self-scattering source is updated from the previous m-th inner iteration. The maximum number of inner iterations is fixed to M. The second term is the down scattering term and it is estimated after performing the prescribed M inner iterations for the first energy group. The third term is the fission source term and it is updated after each outer iteration. The last term is related to the neutron noise source. Thus, all these source terms are known from either the input or the information from the previous iterations, and Eq. (3.13) can be used to compute the spatial distribution of the angular neutron noise $\overline{\delta\psi}_{n,I,J}^{(l,m+1/2)}$ as described in the following.

The sweep starts from the bottom left corner cell of the computational domain. The left surface angular neutron noise $\overline{\delta\psi}^{(\mathrm{l,m+1/2})}_{n,I-1/2,J}(\omega)$ and the bottom surface angular neutron noise $\overline{\delta\psi}^{(\mathrm{l,m+1/2})}_{n,I,J-1/2}(\omega)$ are assumed to be known from the boundary conditions. The right surface angular neutron noise $\overline{\delta\psi}^{(\mathrm{l,m+1/2})}_{n,I+1/2,J}(\omega)$ and the top surface angular neutron noise $\overline{\delta\psi}^{(\mathrm{l,m+1/2})}_{n,I,J+1/2}(\omega)$ are eliminated from Eq. (3.13) by making use of the diamond difference expressions Eqs. (3.11) and (3.12), i.e.

$$\overline{\delta\psi}^{(l,m+1/2)}_{n,I+1/2,J}(\omega) = 2\overline{\delta\psi}^{(l,m+1/2)}_{n,I,J}(\omega) - \overline{\delta\psi}^{(l,m+1/2)}_{n,I-1/2,J}(\omega) \tag{3.22}$$

$$\overline{\delta\psi}^{(l,m+1/2)}_{n,I,J+1/2}(\omega) = 2\overline{\delta\psi}^{(l,m+1/2)}_{n,I,J}(\omega) - \overline{\delta\psi}^{(l,m+1/2)}_{n,I,J-1/2}(\omega) \tag{3.23}$$

Therefore, the cell averaged angular neutron noise $\overline{\delta\psi}^{(l,m+1/2)}_{n,I,J}$ is computed as:

$$\overline{\delta\psi}^{(l,m+1/2)}_{n,I,J}(\omega) = \frac{\left[2\frac{\mu_n}{\Delta x_i}\overline{\delta\psi}^{(l,m+1/2)}_{n,I-1/2,J}(\omega) + 2\frac{\eta_n}{\Delta y_j}\overline{\delta\psi}^{(l,m+1/2)}_{n,I,J-1/2}(\omega) + \bar{q}_{n,I,J}\right]}{\left[\overline{\Sigma^{\mathrm{dyn}}_{\mathrm{t},I,J}} + 2\frac{\mu_n}{\Delta x_I} + 2\frac{\eta_n}{\Delta y_J}\right]} \tag{3.24}$$

In Eq. (3.24), the sum of all the source terms in Eq. (3.13) is denoted by the vector $\bar{q}_{n,I,J}$ and in the solver, the arithmetic operations shown in this equation are done for each group separately. Obtaining the updated cell center neutron noise value from Eq. (3.24) and knowing the values for the left and bottom surfaces, then the neutron noise values at the right and top surface can be determined using Eqs. (3.22) and (3.23). From the initial cell in the bottom-left corner, the algorithm takes, one by one, the cells of the first row along the direction x. When the first row is completed, the algorithm moves to the cells of the next row and repeats the procedure until all the domain is covered. The directions lying in the other quadrants are evaluated with a similar strategy where the sweep follows the direction of neutron travel. Once the sweeps for all the directions are performed, the scalar neutron noise is calculated according to Eq. (3.4), i.e.

$$\overline{\delta\phi}^{(l,m+1)}_{I,J}(\omega) = \frac{\pi}{2}\sum_{\mathrm{n=1}}^{\mathrm{N_0}} w_n \overline{\delta\psi}^{(\mathrm{l,m+1/2})}_{n,I,J}(\omega) \tag{3.25}$$

The self-scattering term in $\bar{q}_{n,I,J}$ is updated for each spatial cell, and one inner iteration is over. The advantage of the transport sweep procedure is that it requires relatively few computational operations in each cell. However, the computational time can be significant for problems with a large number of cells and discrete ordinates. To alleviate this issue, the solver relies on a simple parallelization of the sweeps for different directions.

The inner iterations are embedded into one outer iteration. Accordingly, a prescribed number M of inner iterations are performed for the first energy group. Then the down-scattering term is updated and M inner iterations are also run for the second energy group. After the M inner iterations for both groups, the scalar neutron noise in the fission source term is updated for the next outer iteration:

$$\overline{\delta\phi}_{I,J}^{(l+1,0)}(\omega) = \overline{\delta\phi}_{I,J}^{(l,M)}(\omega) \tag{3.26}$$

In the static module, the iteration procedure is similar but with some differences. In fact, the static module solves an eigenvalue problem without external source. Therefore, after the sweeps are performed for the last energy group, the power iteration method is applied to update k_{eff}, which is part of the fission source term. In the dynamic module, k_{eff} is fixed and the noise source is known, so both do not need to be updated iteratively.

At the end of the outer iteration, the convergence is checked. For the static calculations, the relative differences between the last two iterations for both k_{eff} and the pointwise scalar fluxes are evaluated. In the dynamic module, since the values of the neutron noise are complex quantities, the convergence is checked on the real part, the imaginary part, the amplitude and the phase of the scalar neutron noise. For each of these quantities the relative differences between the last two iterations are calculated pointwise. The iterative process stops when the relative differences are all below a certain predefined value.

3.4 Diffusion synthetic acceleration

The inner-outer iterative scheme can be inefficient and costly in terms of computational effort. To improve the convergence rate of a transport solver, various acceleration methods have been devised. Most of the previous work on acceleration methods has been done for static and time-dependent schemes. The acceleration methods that are most commonly employed in neutron transport codes are the coarse mesh rebalance (CMR) method [10], the diffusion synthetic acceleration (DSA) method [11] and the coarse mesh finite difference (CMFD) method [12]. In all these three methods, the "high-order" transport calculations are accelerated with "low-order" calculations. CMR is one of the first acceleration techniques that were studied. Its performance is very sensitive to how the fine and coarse mesh are chosen. The CMR method suffers from instability problems if too few fine mesh cells are contained in a coarse mesh. On the other hand, it becomes stable but inefficient if the cells of the coarse mesh are large and contains many fine cells. The DSA method has the advantage to be a linear and unconditional stable scheme, but the improvement of the convergence rate may be limited. The CMFD method has recently attracted great interest since, even though it is conditionally stable, its efficiency does not degrade when the coarse mesh size is small. For the acceleration of dynamic transport solvers in the frequency domain, little work is reported in the open literature.

In the current work, the DSA method was investigated as a first attempt to accelerate the 2-energy-group neutron noise algorithm. The derivation and implementation of the DSA equations for the inner and outer iterations of the static module follow closely the work reported in [11] and [13]. The same approach is adapted to the acceleration of the inner and outer iterations of the dynamic module. The general DSA-based scheme is shown in Figure 3.3 and the details are discussed only for the dynamic calculations.

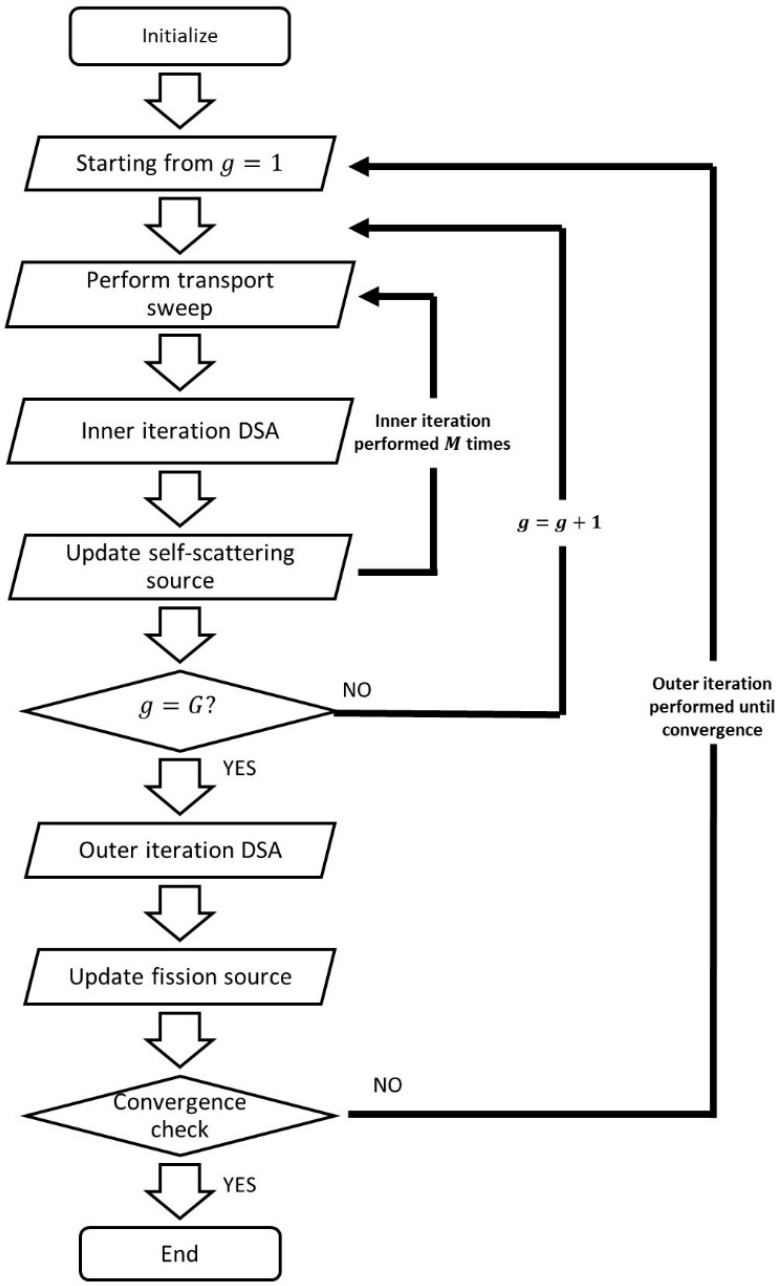

Figure 3.3 The DSA-based scheme for both static and dynamic module of the simulator

The dynamic module starts with the inner iterations, in which Eq. (3.13) is solved for $\overline{\delta\psi}_n^{(l,\mathrm{m}+1/2)}$ and used to update the scalar neutron noise $\overline{\delta\phi}_n^{(l,m+1/2)}$ (instead of $\overline{\delta\phi}_n^{(l,m+1)}$ in the unaccelerated case) with the quadrature formula:

$$\overline{\delta\phi}_{I,J}^{\left(l,m+\frac{1}{2}\right)}(\omega) = \frac{\pi}{2}\sum_{\mathrm{n}=1}^{N_0} w_n \overline{\delta\psi}_{n,I,J}^{\left(l,m+\frac{1}{2}\right)}(\omega) \tag{3.27}$$

In these inner iterations, the estimates of the scalar neutron noise $\overline{\delta\phi}_n^{(l,m+1/2)}$ are adjusted in order to favor convergence. The acceleration step at the $(m+1)$-th inner iteration, within the $(l+1)$-th outer iteration, consists of a low-order diffusion problem that provides the quantities $\delta f_{g,I+1/2,J+1/2}^{(l,m+1)}$ located at cell vertices for the correction of the neutron noise associated with the g-th energy-group, at cell center positions. The discretized equation for the correction quantities reads as:

$$\begin{aligned}
&\frac{2}{\Delta x_I}\left(\Delta y_J D_{g,I,J} + \Delta y_{J+1} D_{g,I,J+1}\right)\left(\delta f_{g,I+1/2,J+1/2}^{(l,m+1)} - \delta f_{g,I-1/2,J+1/2}^{(l,m+1)}\right)\\
&-\frac{2}{\Delta x_{I+1}}\left(\Delta y_J D_{g,I+1,J} + \Delta y_{J+1} D_{g,I+1,J+1}\right)\left(\delta f_{g,I+3/2,J+1/2}^{(l,m+1)} - \delta f_{g,I+1/2,J+1/2}^{(l,m+1)}\right)\\
&+\frac{2}{\Delta y_J}\left(\Delta x_I D_{g,I,J} + \Delta x_{I+1} D_{g,I+1,J}\right)\left(\delta f_{g,I+1/2,J+1/2}^{(l,m+1)} - \delta f_{g,I+1/2,J-1/2}^{(l,m+1)}\right)\\
&-\frac{2}{\Delta y_{J+1}}\left(\Delta x_I D_{g,I,J+1} + \Delta x_{I+1} D_{g,I+1,J+1}\right)\left(\delta f_{g,I+1/2,J+3/2}^{(l,m+1)} - \delta f_{g,I+1/2,J+1/2}^{(l,m+1)}\right)\\
&+\left[\sum_{I'=I}^{I+1}\sum_{J'=J}^{J+1}\left(\Sigma_{R,g,I',J'} V_{I',J'}\right)\right]\delta f_{g,I+1/2,J+1/2}^{(l,m+1)} = \sum_{I'=I}^{I+1}\sum_{J'=J}^{J+1}\Sigma_{ss,g,I',J'} V_{I',J'}\left(\delta\phi_{g,I',J'}^{(l,m+1/2)} - \delta\phi_{g,I',J'}^{(l,m)}\right)
\end{aligned} \tag{3.28}$$

where

$$D_{g,I,J} = \frac{1}{\left(3\Sigma_{t,g,I,J}^{dyn}\right)} \tag{3.29}$$

$$\Sigma_{R,g,I,J} = \Sigma_{t,g,I,J}^{dyn} - \Sigma_{ss,g,I,J} \tag{3.30}$$

Eq. (3.28) is a fixed source problem and by taking all the cell $(I,\ J)$ of the discretized domain, a system of linear equations is built for each energy group, and then it is solved with the LU factorization method. Instead of the update equation used in the unaccelerated scheme (Eq. 3.25) to calculate the scalar neutron noise for next inner iteration, the calculated quantities $\delta f_{g,I+1/2,J+1/2}^{(l,m+1)}$ are used to modify cell center scalar neutron noise as follows:

$$\delta\phi_{g,I,J}^{(l,m+1)} = \delta\phi_{g,I,J}^{\left(l,m+\frac{1}{2}\right)} + \frac{1}{4}\sum_{I'=I}^{I+1}\sum_{J'=J}^{J+1}\delta f_{g,I'-1/2,J'-1/2}^{(l,m+1)} \tag{3.31}$$

The new values given by Eq. (3.31) updates the self-scattering term in Eq. (3.13) before the next inner iteration. As in the unaccelerated case, *M* inner iterations are performed for each energy group.

When the inner iterations are completed for all the energy groups, the calculation continues with the outer iteration. For the acceleration of the $(l+1)$-th outer iteration, the correction quantities $\overline{\delta F}^{(l+1)}_{g,I+1/2,J+1/2}$ for both energy groups are calculated at the cell vertices using the following equation:

$$
\begin{aligned}
&\frac{2}{\Delta x_I}\left(\Delta y_J \overline{\overline{D}}_{I,J} + \Delta y_{J+1}\overline{\overline{D}}_{I,J+1}\right)\left(\overline{\delta F}^{(l+1)}_{I+1/2,J+1/2} - \overline{\delta F}^{(l+1)}_{I-1/2,J+1/2}\right)\\
&-\frac{2}{\Delta x_{I+1}}\left(\Delta y_J \overline{\overline{D}}_{I+1,J} + \Delta y_{J+1}\overline{\overline{D}}_{I+1,J+1}\right)\left(\overline{\delta F}^{(l+1)}_{I+3/2,J+1/2} - \overline{\delta F}^{(l+1)}_{I+1/2,J+1/2}\right)\\
&+\frac{2}{\Delta y_J}\left(\Delta x_I \overline{\overline{D}}_{I,J} + \Delta x_{I+1}\overline{\overline{D}}_{I+1,J}\right)\left(\overline{\delta F}^{(l+1)}_{I+1/2,J+1/2} - \overline{\delta F}^{(l+1)}_{I+1/2,J-1/2}\right)\\
&-\frac{2}{\Delta y_{J+1}}\left(\Delta x_I \overline{\overline{D}}_{I,J+1} + \Delta x_{I+1}\overline{\overline{D}}_{I+1,J+1}\right)\left(\overline{\delta F}^{(l+1)}_{I+1/2,J+3/2} - \overline{\delta F}^{(l+1)}_{I+1/2,J+1/2}\right)\\
&+\left[\sum_{I'=I}^{I+1}\sum_{J'=J}^{J+1}\left(\overline{\overline{\Sigma_R}}_{,I',J'}V_{I',J'}\right)\right]\overline{\delta F}^{(l+1)}_{I+1/2,J+1/2}\\
&-\left[\sum_{I'=I}^{I+1}\sum_{J'=J}^{J+1}\left(\overline{\overline{\Sigma_{sd}}}_{,I',J'}V_{I',J'}\right)\right]\overline{\delta F}^{(l+1)}_{I+\frac{1}{2},J+\frac{1}{2}} = \sum_{I'=I}^{I+1}\sum_{J'=J}^{J+1}\overline{\overline{\chi}}_{I',J'}\,\overline{\overline{\nu\Sigma_f}}_{I',J'}V_{I',J'}\left(\overline{\delta\phi}^{(l,M)}_{I',J'} - \overline{\delta\phi}^{(l)}_{I',J'}\right)
\end{aligned}
\tag{3.32}
$$

with

$$
\overline{\delta F}^{(l+1)}_{I+1/2,J+1/2} = \begin{bmatrix}\delta F^{(l+1)}_{g=1,I+1/2,J+1/2}\\ \delta F^{(l+1)}_{g=2,I+1/2,J+1/2}\end{bmatrix} \tag{3.33}
$$

Eq. (3.32) also represents a fixed source problem where the two energy groups are coupled. Therefore, the linear system constructed for the overall discretized domain, in each outer iteration, includes both energy groups. The calculated values of $\overline{\delta F}^{(l+1)}_{I+1/2,J+1/2}$ are used to correct the neutron noise at cell centers with the following relationship:

$$
\overline{\delta\phi}^{(l+1)}_{I,J} = \overline{\delta\phi}^{(l,M)}_{I,J} + \frac{1}{4}\sum_{I'=I}^{I+1}\sum_{J'=J}^{J+1}\overline{\delta F}^{(l+1)}_{I'-1/2,J'-1/2} \tag{3.34}
$$

Before checking whether the calculation has converged, an updated evaluation of the fission source term of Eq. (3.13) is obtained from the new values of $\overline{\delta\phi}^{(l+1)}_{I,J}$. According to the outcome of the convergence criteria, the calculation is stopped or the next inner-outer iteration is started.

As mentioned above, the accelerated iterative scheme applied in the static and dynamic modules are similar. However, the calculation of the static neutron fluxes requires the update of the value of k_{eff} in the fission source term after every outer iteration, while the neutron noise is determined assuming the value of k_{eff} to be constant and equal to the static one.

Chapter 4

Verification of the neutron noise solver

The performance of the dynamic module in the frequency domain is examined. In Section 4.1, the convergence rate of the unaccelerated and DSA inner-outer iteration schemes for dynamic calculations is studied in the case of an infinite homogeneous system. In Section 4.2, a neutron noise problem in a 2-D heterogeneous system was simulated with the S_N solver and the results are compared with the ones obtained from the diffusion-based solver CORE SIM [4].

4.1 Fourier convergence analysis of the dynamic module

The Fourier convergence analysis method has been widely applied to deterministic neutron transport methods for static calculations [14] and to some extent for time-dependent calculations [15]. The convergence rate of the dynamic module is estimated from the analytical Fourier analysis and compared to numerical results generated by the S_N solver.

In Paper I, the theoretical analysis is based on the one-dimensional continuous form of the iterative equations, while the numerical analysis is performed for a two-dimensional problem. In static calculations, it was shown in [16] that the theoretical results do not depend on the numbers of spatial dimensions when the diamond differencing method is considered. For the dynamic calculations, the same outcome is observed. The Fourier analysis reported below, is based on two-dimensional fully discretized equations.

4.1.1 Spectral radius for the unaccelerated scheme

The 2-dimensional system under study is homogeneous, so cross-sections and kinetic parameters are independent on the spatial position. The spatial discretization is such that the mesh nodes are identical with constant Δx and Δy. The spatial vector that identifies the centre of the node $(I,\ J)$ is defined as:

$$\vec{r} = \left(\left(I - \frac{1}{2}\right)\Delta \mathrm{x}, \left(J - \frac{1}{2}\right)\Delta \mathrm{y}\right), \qquad I = 1, \dots I_{max}, J = 1, \dots, J_{max} \tag{4.1}$$

Additional spatial vectors to locate the surfaces and vertices of the nodes are defined as:

$$\overrightarrow{a_1} = \left(\frac{\Delta x}{2}, 0\right), \qquad \overrightarrow{a_2} = \left(0, \frac{\Delta y}{2}\right) \tag{4.2}$$

Using the notations above, the location of surface with index $(I + 1/2, J)$ can be given by $\vec{r} + \overrightarrow{a_1}$. Similarly, the vertex location with index $(I + 1/2, J + 1/2)$ can be expressed as $\vec{r} + \overrightarrow{a_1} + \overrightarrow{a_2}$.

The errors for the angular neutron noise (at the surfaces or at the center of a cell) and the scalar neutron noise are respectively:

$$\overline{\delta\psi}_n^{\mathrm{err},(l,m+1/2)} = \overline{\delta\psi}_n - \overline{\delta\psi}_n^{(l,m+1/2)} \tag{4.3}$$

and

$$\overline{\delta\phi}_{I,J}^{err,(l,m)} = \overline{\delta\phi}_{I,J} - \overline{\delta\phi}_{I,J}^{(l,m)} \tag{4.4}$$

where $\overline{\delta\psi}_n$ and $\overline{\delta\phi}_{I,J}$ are the exact (or converged) solutions and $\overline{\delta\psi}_n^{(l,m+1/2)}$ and $\overline{\delta\phi}_{I,J}^{(l,m)}$ are the values estimated at the m-th inner iteration, within the $(l+1)$-th outer iteration.

In the case of the unaccelerated scheme, the equation for the error quantities is obtained by subtracting Eq. (3.13) from Eq. (3.6):

$$\begin{aligned}&\frac{\mu_n}{\Delta x}\left[\overline{\delta\psi}_{n,I+1/2,J}^{err,(l,m+1/2)}(\omega) - \overline{\delta\psi}_{n,I-1/2,J}^{err,(l,m+1/2)}(\omega)\right] + \frac{\eta_n}{\Delta y}\left[\overline{\delta\psi}_{n,I,J+1/2}^{err,(l,m+1/2)}(\omega) - \overline{\delta\psi}_{n,I,J-1/2}^{err,(l,m+1/2)}(\omega)\right]\\ &+\overline{\overline{\Sigma_{\mathrm{t},I,J}^{\mathrm{dyn}}}}\,\overline{\delta\psi}_{n,I,J}^{err,(l,m+1/2)}(\omega)\\ &= \frac{1}{2\pi}\overline{\overline{\Sigma_{ss}}}_{I,J}\,\overline{\delta\phi}_{I,J}^{err,(l,m)}(\omega) + \frac{1}{2\pi}\overline{\overline{\Sigma_{sd}}}_{I,J}\,\overline{\delta\phi}_{I,J}^{err,(l,M)}(\omega) + \frac{1}{2\pi}\bar{\bar{\chi}}_{I,J}\,\overline{\overline{\nu\Sigma_f}}_{I,J}\,\overline{\delta\phi}_{I,J}^{err,(l,0)}(\omega)\end{aligned} \tag{4.5}$$

Eq. (4.5) is similar to Eq. (3.13), but the angular and the scalar neutron noise are replaced by the corresponding error quantities and the source term is equal to zero. Then the rate of convergence for the solution of Eq. (3.13) is equivalent to the rate at which the error quantities tend to zero.

In order to study the rate at which the error quantities tend to zero, it is convenient to define the error quantities according to the following Fourier ansatz:

$$\overline{\delta\phi}_{I,J}^{err,(l)}(\vec{r},\omega) = \bar{\bar{A}}^{(l)}(\omega)\bar{b}e^{i\vec{\Theta}\cdot\vec{r}} \tag{4.6}$$

$$\overline{\delta\psi}_{n,I,J}^{\mathrm{err,(l,m+1/2)}}(\vec{r},\omega) = \bar{\bar{A}}^{(l)}(\omega)\bar{\bar{\alpha}}_n^{(l,m)}(\omega)\bar{b}e^{i\vec{\Theta}\cdot\vec{r}} \tag{4.7}$$

$$\overline{\delta\psi}_{n,I+1/2,J}^{\mathrm{err,(l,m+1/2)}}(\vec{r},\omega) = \bar{\bar{A}}^{(l)}(\omega)\bar{\bar{\alpha}}_i^{(l,m)}(\omega)\bar{b}e^{i\vec{\Theta}\cdot(\vec{r}+\overrightarrow{a_1})} \tag{4.8}$$

$$\overline{\delta\psi}_{n,I-1/2,J}^{\mathrm{err,(l,m+1/2)}}(\vec{r},\omega) = \bar{\bar{A}}^{(l)}(\omega)\bar{\bar{\alpha}}_i^{(l,m)}(\omega)\bar{b}e^{i\vec{\Theta}\cdot(\vec{r}-\overrightarrow{a_1})} \tag{4.9}$$

$$\overline{\delta\psi}_{n,I,J+1/2}^{\mathrm{err,(l,m+1/2)}}(\vec{r},\omega) = \bar{\bar{A}}^{(l)}(\omega)\bar{\bar{\alpha}}_j^{(l,m)}(\omega)\bar{b}e^{i\vec{\Theta}\cdot(\vec{r}+\overrightarrow{a_2})} \tag{4.10}$$

$$\overline{\delta\psi}_{n,I,J-1/2}^{\mathrm{err,(l,m+1/2)}}(\vec{r},\omega) = \bar{\bar{A}}^{(l)}(\omega)\bar{\bar{\alpha}}_j^{(l,m)}(\omega)\bar{b}e^{i\vec{\Theta}\cdot(\vec{r}-\overrightarrow{a_2})} \tag{4.11}$$

$$\overline{\delta\phi}_{I,J}^{err,(l,m)}(\vec{r},\omega) = \bar{\bar{A}}^{(l)}(\omega)\bar{\bar{\xi}}_{un,2-D}^{(l,m)}(\omega)\bar{b}e^{i\vec{\Theta}\cdot\vec{r}} \tag{4.12}$$

In Eqs. (4.6) to (4.12), $\vec{\Theta} = (\Theta_1, \Theta_2)$ is the Fourier error mode. It consists of two components that are, respectively, the error modes in the x and y directions and can take any values in the interval $[-\infty, +\infty]$. The elements of the column vector $\bar{b}$ are equal to 1. The matrix $\bar{\bar{A}}^{(l)}$ is diagonal and each element of the diagonal is associated with the error for one neutron energy group, after the l-th outer iteration. The matrices $\bar{\bar{\alpha}}_n^{(l,m)}$, $\bar{\bar{\alpha}}_i^{(l,m)}$, $\bar{\bar{\alpha}}_j^{(l,m)}$ and $\bar{\bar{\xi}}_{un,2-D}^{(l,m)}$ are diagonal

matrices, and each element of the diagonal is associated with the error for one neutron energy group at the m-th inner iteration, within the $(l+1)$-th outer iteration.

The convergence rate is related to the variation of the matrix $\bar{\bar{A}}$ between the two successive outer iterations l and $l+1$. This variation depends on the properties of the matrix $\bar{\bar{\xi}}_{un,2-D}^{(l,m)}$. In fact, once all the prescribed M inner iterations are performed within the $(l+1)$-th outer iteration, the error $\overline{\delta\phi}_{I,J}^{err,(l,M)}$ given by Eq. (4.12) is equal to the error $\overline{\delta\phi}_{I,J}^{err,(l+1)}$ given by Eq. (4.6) at the end of the $(l+1)$-th outer iteration, i.e.:

$$\bar{\bar{A}}^{(l+1)} = \bar{\bar{A}}^{(l)}(\omega)\bar{\bar{\xi}}_{un,2-D}^{(l,M)} \tag{4.13}$$

For the determination of $\bar{\bar{\xi}}_{un,2-D}^{(l,M)}$, the Fourier ansatz is entered in Eq. (4.5) and $e^{i\vec{\Theta}\cdot\vec{r}}$ is eliminated from all the terms. The expressions:

$$e^{i\vec{\Theta}\cdot\overrightarrow{a_1}} - e^{-i\vec{\Theta}\cdot\overrightarrow{a_1}} = 2i\sin\left(\Theta_1\frac{\Delta x}{2}\right) \tag{4.14}$$

$$e^{i\vec{\Theta}\cdot\overrightarrow{a_2}} - e^{-i\vec{\Theta}\cdot\overrightarrow{a_2}} = 2i\sin\left(\Theta_2\frac{\Delta y}{2}\right) \tag{4.15}$$

are used in the first two terms of the left-hand side, so that the equation is rewritten as:

$$\frac{\mu_n}{\Delta x}\bar{\bar{\alpha}}_i^{(l,m)}2i\sin\left(\Theta_1\frac{\Delta x}{2}\right) + \frac{\eta_n}{\Delta y}\bar{\bar{\alpha}}_j^{(l,m)}2i\sin\left(\Theta_2\frac{\Delta y}{2}\right) + \overline{\overline{\Sigma_t^{dyn}}}\,\bar{\bar{\alpha}}_n^{(l,m)} = \frac{1}{2\pi}\overline{\overline{\Sigma_{ss}}}\,\bar{\bar{\xi}}_{un,2-D}^{(l,m)} + \frac{1}{2\pi}\overline{\overline{\Sigma_{sd}}}\,\bar{\bar{\xi}}_{un,2-D}^{(l,M)} + \frac{1}{2\pi}\bar{\bar{\chi}}\,\overline{\overline{\nu\Sigma_f}} \tag{4.16}$$

The coefficient matrices $\bar{\bar{\alpha}}_i^{(l,m)}$ and $\bar{\bar{\alpha}}_j^{(l,m)}$ are replaced with $\bar{\bar{\alpha}}_n^{(l,m)}$ through the relationships derived from the diamond difference scheme:

$$\bar{\bar{\alpha}}_n^{(l,m)} = \frac{1}{2}\bar{\bar{\alpha}}_i^{(l,m)}\left(e^{i\vec{\Theta}\cdot\overrightarrow{a_1}} + e^{-i\vec{\Theta}\cdot\overrightarrow{a_1}}\right) = \bar{\bar{\alpha}}_i^{(l,m)}\cos\left(\Theta_1\frac{\Delta x}{2}\right) \tag{4.17}$$

$$\bar{\bar{\alpha}}_n^{(l,m)} = \frac{1}{2}\bar{\bar{\alpha}}_j^{(l,m)}\left(e^{i\vec{\Theta}\cdot\overrightarrow{a_2}} + e^{-i\vec{\Theta}\cdot\overrightarrow{a_2}}\right) = \bar{\bar{\alpha}}_j^{(l,m)}\cos\left(\Theta_2\frac{\Delta y}{2}\right) \tag{4.18}$$

As a result, Eq. (4.16) becomes:

$$\frac{\mu_n}{\Delta x}\bar{\bar{\alpha}}_n^{(l,m)}2i\tan\left(\Theta_1\frac{\Delta x}{2}\right) + \frac{\eta_n}{\Delta y}\bar{\bar{\alpha}}_n^{(l,m)}2i\tan\left(\Theta_2\frac{\Delta y}{2}\right) + \overline{\overline{\Sigma_t^{dyn}}}\,\bar{\bar{\alpha}}_n^{(l,m)} = \frac{1}{2\pi}\overline{\overline{\Sigma_{ss}}}\,\bar{\bar{\xi}}_{un,2-D}^{(l,m)} + \frac{1}{2\pi}\overline{\overline{\Sigma_{sd}}}\,\bar{\bar{\xi}}_{un,2-D}^{(l,M)} + \frac{1}{2\pi}\bar{\bar{\chi}}\,\overline{\overline{\nu\Sigma_f}} \tag{4.19}$$

Isolating $\bar{\bar{\alpha}}_n^{(l,m)}$ leads to:

$$\bar{\bar{\alpha}}_n^{(l,m)} = \frac{1}{2\pi}\cdot\frac{\overline{\overline{\Sigma_{ss}}}\,\bar{\bar{\xi}}_{un,2-D}^{(l,m)} + \overline{\overline{\Sigma_{sd}}}\,\bar{\bar{\xi}}_{un,2-D}^{(l,M)} + \bar{\bar{\chi}}\,\overline{\overline{\nu\Sigma_f}}}{\frac{\mu_n}{\Delta x}2i\tan\left(\Theta_1\frac{\Delta x}{2}\right) + \frac{\eta_n}{\Delta y}2i\tan\left(\Theta_2\frac{\Delta y}{2}\right) + \overline{\overline{\Sigma_t^{dyn}}}} \tag{4.20}$$

This equation contains $\bar{\bar{\alpha}}_n$ and $\bar{\bar{\xi}}^{(l,m)}_{un,2-D}$, so a second relationship is necessary to eliminate $\bar{\bar{\alpha}}_n$. For this purpose, the error of the scalar neutron noise is expressed as a function of the error of the angular neutron noise via a quadrature formula derived from Eqs. (3.25), (4.3) and (4.4):

$$\overline{\delta\phi}^{err,(l,m+1)}_{I,J}(\omega) = \frac{\pi}{2}\sum_{\mathrm{n}=1}^{\mathrm{N_0}} \mathrm{w_n}\overline{\delta\psi}^{err,(\mathrm{l,m+1/2})}_{n,I,J}(\omega) \tag{4.21}$$

Eq. (4.21) in combination with Eqs. (4.7) and (4.12) yields the additional relationship between $\bar{\bar{\alpha}}_n$ and $\bar{\bar{\xi}}^{(l,m)}_{un,2-D}$, i.e.:

$$\bar{\bar{\xi}}^{(l,m+1)}_{un,2-D} = \frac{\pi}{2}\sum_{\mathrm{n}=1}^{\mathrm{N_0}} \mathrm{w_n}\bar{\bar{\alpha}}^{(l,m)}_n \tag{4.22}$$

Both sides of Eq. (4.20) are multiplied by $\frac{\pi}{2}w_n$ and the summation over n is taken, so the left-hand side will be equal to the right-hand side of Eq. (4.22) and an expression for the matrix $\bar{\bar{\xi}}^{(l,m)}_{un,2-D}$ is found, which reads as:

$$\bar{\bar{\xi}}^{(l,m+1)}_{un,2-D} = \frac{\pi}{2}\sum_{\mathrm{n}=1}^{\mathrm{N_0}} \mathrm{w_n}\frac{\frac{1}{2\pi}\overline{\overline{\Sigma_{ss}}}\bar{\bar{\xi}}^{(l,m)} + \frac{1}{2\pi}\overline{\overline{\Sigma_{sd}}}\,\bar{\bar{\xi}}^{(l,M)} + \frac{1}{2\pi}\bar{\bar{\chi}}\,\overline{\overline{\nu\Sigma_{\mathrm{f}}}}}{\frac{\mu_n}{\Delta x}2i\tan\left(\Theta_1\frac{\Delta x}{2}\right) + \frac{\eta_n}{\Delta y}2i\tan\left(\Theta_2\frac{\Delta y}{2}\right) + \overline{\overline{\Sigma_t^{dyn}}}} \tag{4.23}$$

Eq. (4.23) can be arranged in a more compact form as follows (being $m = M$):

$$\bar{\bar{\xi}}^{(l,M)}_{un,2-D} = \left[\bar{\bar{I}} - \left(\bar{\bar{I}} - \bar{\bar{P}}\right)^{-1}\left(\bar{\bar{I}} - \bar{\bar{P}}^{M}\right)\bar{\bar{Q}}\right]^{-1}\left[\bar{\bar{P}}^{M} + \left(\bar{\bar{I}} - \bar{\bar{P}}\right)^{-1}\left(\bar{\bar{I}} - \bar{\bar{P}}^{M}\right)\bar{\bar{R}}\right] \tag{4.24}$$

with

$$\bar{\bar{P}} = \bar{\bar{T}}\overline{\overline{\Sigma_t^{dyn}}}^{-1}\overline{\overline{\Sigma_{ss}}} \tag{4.25}$$

$$\bar{\bar{Q}} = \bar{\bar{T}}\overline{\overline{\Sigma_t^{dyn}}}^{-1}\overline{\overline{\Sigma_{sd}}} \tag{4.26}$$

$$\bar{\bar{R}} = \bar{\bar{T}}\overline{\overline{\Sigma_t^{dyn}}}^{-1}\bar{\bar{\chi}}\,\overline{\overline{\nu\Sigma_{\mathrm{f}}}} \tag{4.27}$$

$$\bar{\bar{T}} = \sum_{\mathrm{n}=1}^{\mathrm{N_0}}\frac{1}{4}\mathrm{w_n}\left\{\left[2i\frac{\mu_{\mathrm{n}}}{\Delta \mathrm{x}}\tan\left(\Theta_1\frac{\Delta x}{2}\right) + 2i\frac{\eta_{\mathrm{n}}}{\Delta \mathrm{y}}\tan\left(\Theta_2\frac{\Delta y}{2}\right)\right]\overline{\overline{\Sigma_t^{dyn}}}^{-1} + \bar{\bar{I}}\right\}^{-1} \tag{4.28}$$

and $\bar{\bar{I}}$ is the identity matrix.

The spectral radius of the unaccelerated scheme, denoted as ρ, is equal to the maximum among the absolute values of the eigenvalues of the matrix $\bar{\bar{\xi}}^{(l,M)}_{un,2-D}\left(\omega,\vec{\Theta}\right)$, given any possible values of Θ_1 and Θ_2, i.e.:

$$\rho\left(\omega, M, \vec{\Theta}\right) = max\left\{abs\left[eig\left(\bar{\bar{\xi}}^{(l,M)}_{un,2-D}\left(\omega,\vec{\Theta}\right)\right)\right]\right\} \tag{4.29}$$

The rate at which the error quantities tend to zero and thus the rate at which the unaccelerated scheme converges can then be determined by taking the maximum of ρ over all possible error modes:

$$rate\ of\ convergence = \max_{-\infty<\Theta_1,\Theta_2<+\infty}(\rho) \tag{4.30}$$

4.1.2 Spectral radius of the DSA scheme

As shown in Eqs. (3.27) to (3.34), the DSA algorithm is such that two quantities $\overline{\delta f}$ and $\overline{\delta F}$ are used to adjust and thus accelerate respectively the inner and the outer iterations of the neutron noise calculation. Analogous to the unaccelerated case, the theoretical convergence rate is derived for the two-dimensional scheme.

First the part of the algorithm that includes the inner iterations is considered. An inner iteration starts with the transport sweep based on Eq. (3.13). This operation is common in the unaccelerated and DSA schemes, hence error quantities like those that fulfil Eq. (4.5) in the unaccelerated case, can be defined. The Fourier ansatz for the error quantities associated with the transport sweep of the accelerated solver, is formalized as:

$$\overline{\delta\phi}_{I,J}^{err,acc,(l)}(\vec{r},\omega) = \bar{\bar{A}}^{acc,(l)}(\omega)\bar{b}e^{i\vec{\Theta}\cdot\vec{r}} \tag{4.31}$$

$$\overline{\delta\psi}_{n,I,J}^{err,acc,(l,m+1/2)}(\vec{r},\omega) = \bar{\bar{A}}^{acc,(l)}(\omega)\bar{\bar{\alpha}}_n^{acc,(l,m)}(\omega)\bar{b}e^{i\vec{\Theta}\cdot\vec{r}} \tag{4.32}$$

$$\overline{\delta\psi}_{n,I+1/2,J}^{err,acc,(l,m+1/2)}(\vec{r},\omega) = \bar{\bar{A}}^{acc,(l)}(\omega)\bar{\bar{\alpha}}_i^{acc,(l,m)}(\omega)\bar{b}e^{i\vec{\Theta}\cdot(\vec{r}+\overrightarrow{a_1})} \tag{4.33}$$

$$\overline{\delta\psi}_{n,I-1/2,J}^{err,acc,(l,m+1/2)}(\vec{r},\omega) = \bar{\bar{A}}^{acc,(l)}(\omega)\bar{\bar{\alpha}}_i^{acc,(l,m)}(\omega)\bar{b}e^{i\vec{\Theta}\cdot(\vec{r}-\overrightarrow{a_1})} \tag{4.34}$$

$$\overline{\delta\psi}_{n,I,J+1/2}^{err,acc,(l,m+1/2)}(\vec{r},\omega) = \bar{\bar{A}}^{acc,(l)}(\omega)\bar{\bar{\alpha}}_j^{acc,(l,m)}(\omega)\bar{b}e^{i\vec{\Theta}\cdot(\vec{r}+\overrightarrow{a_2})} \tag{4.35}$$

$$\overline{\delta\psi}_{n,I,J-1/2}^{err,acc,(l,m+1/2)}(\vec{r},\omega) = \bar{\bar{A}}^{acc,(l)}(\omega)\bar{\bar{\alpha}}_j^{acc,(l,m)}(\omega)\bar{b}e^{i\vec{\Theta}\cdot(\vec{r}-\overrightarrow{a_2})} \tag{4.36}$$

$$\overline{\delta\phi}_{I,J}^{err,acc,(l,m)}(\vec{r},\omega) = \bar{\bar{A}}^{acc,(l)}(\omega)\bar{\bar{\xi}}_{2-D}^{acc,(l,m)}(\omega)\bar{b}e^{i\vec{\Theta}\cdot\vec{r}} \tag{4.37}$$

The matrices $\bar{\bar{A}}^{acc,(l)}(\omega)$, $\bar{\bar{\alpha}}^{acc,(l,m)}$ and $\bar{\bar{\xi}}_{2-D}^{acc,(l,m)}$ are similar to the matrices used in Eqs. (4.6) to (4.12) for the unaccelerated problem. The procedure used to obtain Eq. (4.20) from Eq. (4.5), can be adapted to the accelerated case in such a manner that yields:

$$\bar{\bar{\alpha}}_n^{acc,(l,m)} = \frac{\frac{1}{2\pi}\overline{\overline{\Sigma_{ss}}}\,\bar{\bar{\xi}}_{2-D}^{acc,(l,m)} + \frac{1}{2\pi}\overline{\overline{\Sigma_{sd}}}\,\bar{\bar{\xi}}_{2-D}^{acc,(l,M)} + \frac{1}{2\pi}\bar{\bar{\chi}}\,\overline{\overline{\nu\Sigma_f}}}{\frac{\mu_n}{\Delta x}2i\,tan\left(\Theta_1\frac{\Delta x}{2}\right) + \frac{\eta_n}{\Delta y}2i\,tan\left(\Theta_2\frac{\Delta y}{2}\right) + \overline{\overline{\Sigma_t^{dyn}}}} \tag{4.38}$$

The transport sweep gives the angular neutron noise that is required in Eq. (3.27) to estimate the scalar neutron noise. This estimation identified by the iteration index $(m+1/2)$, is corrected according to the DSA method before it can be used to update the next inner iteration. Therefore, differently from the unaccelerated scheme, an error is also specified for this scalar neutron noise, i.e.:

$$\overline{\delta\phi}_{I,J}^{err,acc,(l,m+1/2)} = \overline{\delta\phi}_{I,J} - \overline{\delta\phi}_{I,J}^{(l,m+1/2)} \tag{4.39}$$

The Fourier ansatz relative to $\overline{\delta\phi}_{I,J}^{err,acc,(l,m+1/2)}$ reads as:

$$\overline{\delta\phi}_{I,J}^{err,acc,(l,m+1/2)}(\vec{r},\omega) = \bar{\bar{A}}^{acc,(l)}(\omega)\bar{\bar{\beta}}^{(l,m)}(\omega)\bar{b}e^{i\vec{\Theta}\cdot\vec{r}} \tag{4.40}$$

were $\bar{\bar{\beta}}^{(l,m)}$ is a diagonal matrix in which each element of the diagonal is connected to the error for one neutron energy group at the the m-th inner iteration, within the $(l+1)$-th outer iteration.

From Eq. (3.27) and the definitions of the errors $\overline{\delta\phi}_{I,J}^{err,acc,(l,m+1/2)}$ and $\overline{\delta\psi}_{n,I,J}^{err,acc,(\mathrm{l,m+1/2})}$, the following expression is obtained:

$$\overline{\delta\phi}_{I,J}^{err,acc,(l,m+1/2)}(\omega) = \frac{\pi}{2}\sum_{\mathrm{n=1}}^{\mathrm{N_0}} w_n \overline{\delta\psi}_{n,I,J}^{err,acc,(\mathrm{l,m+1/2})}(\omega) \tag{4.41}$$

The combination of Eqs. (4.41), (4.32) and (4.40) leads to:

$$\bar{\bar{\beta}}^{(l,m)} = \frac{\pi}{2}\sum_{\mathrm{n=1}}^{\mathrm{N_0}} w_n \bar{\bar{\alpha}}_n^{acc,(l,m)} \tag{4.42}$$

Eq. (4.42) is substituted in Eq. (4.38), so that a relationship between $\bar{\bar{\beta}}^{(l,m)}$ and $\bar{\bar{\xi}}_{2-D}^{acc,(l,m)}$ is derived:

$$\bar{\bar{\beta}}^{(l,m)} = \frac{\pi}{2}\sum_{n=1}^{N} w_n \frac{\frac{1}{2\pi}\overline{\overline{\Sigma_{ss}}}\bar{\bar{\xi}}_{2-D}^{acc,(l,m)} + \frac{1}{2\pi}\overline{\overline{\Sigma_{sd}}}\,\bar{\bar{\xi}}_{2-D}^{acc,(l,M)} + \frac{1}{2\pi}\bar{\bar{\chi}}\,\overline{\overline{\nu\Sigma_f}}}{\frac{\mu_n}{\Delta x}2i\,tan\left(\Theta_1\frac{\Delta x}{2}\right) + \frac{\eta_n}{\Delta y}2i\,tan\left(\Theta_2\frac{\Delta y}{2}\right) + \overline{\overline{\Sigma_t^{dyn}}}} \tag{4.43}$$

The numerical acceleration is such that the estimation $\overline{\delta\phi}_{I,J}^{(l,m+1/2)}$ is corrected with the factor $\overline{\delta f}$. Then an error quantity $\overline{\delta f}^{err}$ is defined as the difference between the converged correction factor $\overline{\delta f}$ and $\overline{\delta f}^{(l,m)}$ after one inner iteration. The equation for this error quantity at a certain inner iteration $(m+1)$, within the $(l+1)$-th outer iteration, is formally derived from the difference between the DSA inner equation (Eq. (3.28)) written for the converged solution (although the converged value of $\overline{\delta f}$ is zero) and for the inner iteration of interest, i.e.:

$$\begin{aligned}
&\frac{2}{\Delta x_I}\left(\Delta y_J\bar{\bar{D}}_{I,J} + \Delta y_{J+1}\bar{\bar{D}}_{I,J+1}\right)\left(\overline{\delta f}_{I+1/2,J+1/2}^{err,(l,m+1)} - \overline{\delta f}_{I-1/2,J+1/2}^{err,(l,m+1)}\right)\\
&-\frac{2}{\Delta x_{I+1}}\left(\Delta y_J\bar{\bar{D}}_{I+1,J} + \Delta y_{J+1}\bar{\bar{D}}_{I+1,J+1}\right)\left(\overline{\delta f}_{I+3/2,J+1/2}^{err,(l,m+1)} - \overline{\delta f}_{I+1/2,J+1/2}^{err,(l,m+1)}\right)\\
&+\frac{2}{\Delta y_J}\left(\Delta x_I\bar{\bar{D}}_{I,J} + \Delta x_{I+1}\bar{\bar{D}}_{I+1,J}\right)\left(\overline{\delta f}_{I+1/2,J+1/2}^{err,(l,m+1)} - \overline{\delta f}_{I+1/2,J-1/2}^{err,(l,m+1)}\right)\\
&+\frac{2}{\Delta y_{J+1}}\left(\Delta x_I\bar{\bar{D}}_{I,J+1} + \Delta x_{I+1}\bar{\bar{D}}_{I+1,J+1}\right)\left(\overline{\delta f}_{I+1/2,J+3/2}^{err,(l,m+1)} - \overline{\delta f}_{I+1/2,J+1/2}^{err,(l,m+1)}\right)\\
&+\left[\sum_{I'=I}^{I+1}\sum_{J'=J}^{J+1}\left(\overline{\overline{\Sigma_R}}_{,I',J'}V_{I',J'}\right)\right]\overline{\delta f}_{I+\frac{1}{2},J+\frac{1}{2}}^{err,(l,m+1)}\\
&=\sum_{I'=I}^{I+1}\sum_{J'=J}^{J+1}\overline{\overline{\Sigma_{ss}}}_{,I',J'}V_{I',J'}\left(\overline{\delta\phi}_{I',J'}^{err,acc,\left(l,m+\frac{1}{2}\right)} - \overline{\delta\phi}_{I',J'}^{err,acc,(l,m)}\right)
\end{aligned} \tag{4.44}$$

Eq. (4.44) relates the values of $\overline{\overline{\delta f}}^{err}$ at the 5 vertices $(I+1/2, J+1/2), (I+1/2, J-1/2), (I-1/2, J+1/2), (I+3/2, J+1/2)$ and $(I+1/2, J+3/2)$. The Fourier ansatz used for them is the following one:

$$\overline{\delta f}^{err,(l,m+1)}_{I+1/2,J+1/2}(\overrightarrow{r,\omega}) = \bar{\bar{A}}^{acc,(l)}(\omega)\bar{\bar{\gamma}}^{(l,m)}(\omega)\bar{b}e^{i\vec{\Theta}\cdot(\vec{r}+\overrightarrow{a_1}+\overrightarrow{a_2})} \quad (4.45)$$

$$\overline{\delta f}^{err,(l,m+1)}_{I-1/2,J+1/2}(\vec{r},\omega) = \bar{\bar{A}}^{acc,(l)}(\omega)\bar{\bar{\gamma}}^{(l,m)}(\omega)\bar{b}e^{i\vec{\Theta}\cdot(\vec{r}-\overrightarrow{a_1}+\overrightarrow{a_2})} \quad (4.46)$$

$$\overline{\delta f}^{err,(l,m+1)}_{I+1/2,J-1/2}(\vec{r},\omega) = \bar{\bar{A}}^{acc,(l)}(\omega)\bar{\bar{\gamma}}^{(l,m)}(\omega)\bar{b}e^{i\vec{\Theta}\cdot(\vec{r}+\overrightarrow{a_1}-\overrightarrow{a_2})} \quad (4.47)$$

$$\overline{\delta f}^{err,(l,m+1)}_{I+1/2,J+3/2}(\vec{r},\omega) = \bar{\bar{A}}^{acc,(l)}(\omega)\bar{\bar{\gamma}}^{(l,m)}(\omega)\bar{b}e^{i\vec{\Theta}\cdot(\vec{r}+\overrightarrow{a_1}+3\overrightarrow{a_2})} \quad (4.48)$$

$$\overline{\delta f}^{err,(l,m+1)}_{I+3/2,J+1/2}(\vec{r},\omega) = \bar{\bar{A}}^{acc,(l)}(\omega)\bar{\bar{\gamma}}^{(l,m)}(\omega)\bar{b}e^{i\vec{\Theta}\cdot(\vec{r}+3\overrightarrow{a_1}+\overrightarrow{a_2})} \quad (4.49)$$

In Eq. (4.44), the error quantities $\overline{\delta\phi}^{err,acc,(l,m+1/2)}_{I',J'}$ and $\overline{\delta\phi}^{err,acc,(l,m)}_{I',J'}$, whose definition and Fourier ansatz are introduced above, also appear.

Inserting Eqs. (4.45) to (4.49), (4.37) and (4.40) into Eq. (4.44) leads to a relationship for the matrices $\bar{\bar{\xi}}^{acc,(l,m)}_{2-D}$, $\bar{\bar{\gamma}}^{(l,m)}$ and $\bar{\bar{\beta}}^{(l,m)}$, i.e.:

$$\bar{\bar{\gamma}}^{(l,m)} = \bar{\bar{L}}\cdot\ a\cdot\left(\bar{\bar{\beta}}^{(l,m)} - \bar{\bar{\xi}}^{acc,(l,m)}_{2-D}\right) \quad (4.50)$$

The matrix $\bar{\bar{L}}$ and coefficient a are respectively equal to:

$$\bar{\bar{L}} = \Delta x\Delta y\left[4\frac{\Delta y}{\Delta x}\bar{\bar{D}}(1-\cos\Theta_1\Delta x) + 4\frac{\Delta x}{\Delta y}\bar{\bar{D}}(1-\cos\Theta_2\Delta y) + 2\overline{\overline{\Sigma_R}}\Delta x\Delta y\right]^{-1}\overline{\overline{\Sigma_{ss}}} \quad (4.51)$$

$$a = \cos\left(\frac{\Theta_1\Delta x}{2}+\frac{\Theta_2\Delta y}{2}\right) + \cos\left(\frac{\Theta_1\Delta x}{2}-\frac{\Theta_2\Delta y}{2}\right) \quad (4.52)$$

An alternative relationship between $\bar{\bar{\xi}}^{acc,(l,m)}_{2-D}$, $\bar{\bar{\gamma}}^{(l,m)}$ and $\bar{\bar{\beta}}^{(l,m)}$ is built from Eq. (3.31) that updates the scalar neutron noise in the accelerated inner iterations. Eq. (3.31) together with the definition of $\overline{\overline{\delta f}}^{err}$ and $\overline{\overline{\delta\phi}}^{err}$, gives:

$$\overline{\delta\phi}^{err,acc,(l,m+1)}_{I,J} = \overline{\delta\phi}^{err,acc,\left(l,m+\frac{1}{2}\right)}_{I,J} + \frac{1}{4}\sum_{I'=I}^{I+1}\sum_{J'=J}^{J+1}\overline{\delta f}^{err,(l,m+1)}_{I'-1/2,J'-1/2} \quad (4.53)$$

Eqs. (4.37), (4.40) and (4.45) to (4.49) are inserted into Eq. (4.53) and the second relationship for $\bar{\bar{\xi}}^{acc,(l,m+1)}_{2-D}$, $\bar{\bar{\gamma}}^{(l,m)}$ and $\bar{\bar{\beta}}^{(l,m)}$ is obtained:

$$\bar{\bar{\xi}}^{acc,(l,m+1)}_{2-D} = \bar{\bar{\beta}}^{(l,m)} + \frac{a}{2}\bar{\bar{\gamma}}^{(l,m)} \quad (4.54)$$

Then, $\bar{\bar{\xi}}^{acc,(l,M)}_{2-D}$ can be determined with an expression that is derived from Eqs. (4.43), (4.50) and (4.54), and that reads as:

$$\bar{\bar{\xi}}^{acc,(l,M)}_{2-D} = \left[\bar{\bar{I}} - \left(\bar{\bar{I}} - \overline{\overline{P^{acc}}}\right)^{-1}\left(\bar{\bar{I}} - \overline{\overline{P^{acc}}}\right)\overline{\overline{Q^{acc}}}\right]^{-1}\left[\overline{\overline{P^{acc}}}^{M} + \left(\bar{\bar{I}} - \overline{\overline{P^{acc}}}\right)^{-1}\left(\bar{\bar{I}} - \overline{\overline{P^{acc}}}^{M}\right)\overline{\overline{R^{acc}}}\right] \quad (4.55)$$

with

$$\overline{\overline{P^{acc}}} = \bar{\bar{T}}\,\overline{\overline{\Sigma_t^{dyn}}}^{-1}\overline{\overline{\Sigma_{ss}}} + \frac{a^2}{2}\bar{\bar{L}}\left(\bar{\bar{T}}\,\overline{\overline{\Sigma_t^{dyn}}}^{-1}\overline{\overline{\Sigma_{ss}}} - \bar{\bar{I}}\right) \tag{4.56}$$

$$\overline{\overline{Q^{acc}}} = \bar{\bar{T}}\,\overline{\overline{\Sigma_t^{dyn}}}^{-1}\overline{\overline{\Sigma_{sd}}} + \frac{a^2}{2}\bar{\bar{L}}\bar{\bar{T}}\,\overline{\overline{\Sigma_t^{dyn}}}^{-1}\overline{\overline{\Sigma_{sd}}} \tag{4.57}$$

$$\overline{\overline{R^{acc}}} = \bar{\bar{T}}\,\overline{\overline{\Sigma_t^{dyn}}}^{-1}\bar{\bar{\chi}}\,\overline{\overline{\nu\Sigma_{\mathrm{f}}}} + \frac{a^2}{2}\bar{\bar{L}}\bar{\bar{T}}\,\overline{\overline{\Sigma_t^{dyn}}}^{-1}\bar{\bar{\chi}}\,\overline{\overline{\nu\Sigma_{\mathrm{f}}}} \tag{4.58}$$

The matrix $\bar{\bar{T}}$ is specified in Eq. (4.28). The maximum spectral radius of the matrix given in Eq. (4.55) represents the convergence rate of the scheme with DSA-based inner iterations and unaccelerated outer iterations.

For the convergence analysis of the full DSA scheme, the part related to the outer iterations also needs to be taken in account. Then an error quantity $\overline{\delta F}^{err}$ is defined for the correction factor $\overline{\delta F}$ used to accelerate the outer iterations. This error is formally equal to the difference between the converged value (which is zero) and the value at a certain outer iteration. Subtracting the DSA outer equation (Eq. (3.32)) for the $(l+1)$-th outer iteration from Eq. (3.32) written for the converged solution yields:

$$\begin{aligned}
&\frac{2}{\Delta x_I}\left(\Delta y_J\bar{\bar{D}}_{I,J} + \Delta y_{J+1}\bar{\bar{D}}_{I,J+1}\right)\left(\overline{\delta F}^{err,(l+1)}_{I+1/2,J+1/2} - \overline{\delta F}^{err,(l+1)}_{I-1/2,J+1/2}\right)\\
&-\frac{2}{\Delta x_{I+1}}\left(\Delta y_J\bar{\bar{D}}_{I+1,J} + \Delta y_{J+1}\bar{\bar{D}}_{I+1,J+1}\right)\left(\overline{\delta F}^{err,(l+1)}_{I+3/2,J+1/2} - \overline{\delta F}^{err,(l+1)}_{I+1/2,J+1/2}\right)\\
&+\frac{2}{\Delta y_J}\left(\Delta x_I\bar{\bar{D}}_{I,J} + \Delta x_{I+1}\bar{\bar{D}}_{I+1,J}\right)\left(\overline{\delta F}^{err,(l+1)}_{I+1/2,J+1/2} - \overline{\delta F}^{err,(l+1)}_{I+1/2,J-1/2}\right)\\
&+\frac{2}{\Delta y_{J+1}}\left(\Delta x_I\bar{\bar{D}}_{I,J+1} + \Delta x_{I+1}\bar{\bar{D}}_{I+1,J+1}\right)\left(\overline{\delta F}^{err,(l+1)}_{I+1/2,J+3/2} - \overline{\delta F}^{err,(l+1)}_{I+1/2,J+1/2}\right)\\
&+\left[\sum_{I'=I}^{I+1}\sum_{J'=J}^{J+1}\left(\overline{\overline{\Sigma_R}}_{,I',J'}V_{I',J'}\right)\right]\overline{\delta F}^{err,(l+1)}_{I+1/2,J+1/2} - \sum_{I'=I}^{I+1}\sum_{J'=J}^{J+1}\left(\overline{\overline{\Sigma_{sd}}}_{,I',J'}V_{I',J'}\right)\overline{\delta F}^{err,(l+1)}_{I+\frac{1}{2},J+\frac{1}{2}}\\
&=\sum_{I'=I}^{I+1}\sum_{J'=J}^{J+1}\bar{\bar{\chi}}_{\mathrm{I}',\mathrm{J}'}\,\overline{\overline{\nu\Sigma_{\mathrm{f}}}}_{\mathrm{I}',\mathrm{J}'}V_{I',J'}\left(\overline{\delta\phi}^{err,acc,(l,M)}_{I',J'} - \overline{\delta\phi}^{err,acc,(l)}_{I',J'}\right)
\end{aligned} \tag{4.59}$$

where $\overline{\delta\phi}^{err,acc}$ denotes the error of the scalar neutron noise, as discussed above. Similar to the case of $\overline{\delta f}^{err}$ in Eq. (4.44), the error quantity $\overline{\delta F}^{err}$ is given at the 5 vertices $(I+1/2, J+1/2), (I+1/2, J-1/2), (I-1/2, J+1/2), (I+3/2, J+1/2)$ and $(I+1/2, J+3/2)$ and the associated Fourier ansatz is formulated as:

$$\overline{\delta F}^{err,(l+1)}_{I+1/2,J+1/2}(\vec{r},\omega) = \bar{\bar{A}}^{acc,(l)}(\omega)\bar{\bar{\vartheta}}^{(l)}(\omega)\bar{b}e^{i\vec{\Theta}\cdot(\vec{r}+\overrightarrow{a_1}+\overrightarrow{a_2})} \tag{4.60}$$

$$\overline{\delta F}^{err,(l+1)}_{I-1/2,J+1/2}(\vec{r},\omega) = \bar{\bar{A}}^{acc,(l)}(\omega)\bar{\bar{\vartheta}}^{(l)}(\omega)\bar{b}e^{i\vec{\Theta}\cdot(\vec{r}-\overrightarrow{a_1}+\overrightarrow{a_2})} \tag{4.61}$$

$$\overline{\delta F}^{err,(l+1)}_{I+1/2,J-1/2}(\vec{r},\omega) = \bar{\bar{A}}^{acc,(l)}(\omega)\bar{\bar{\vartheta}}^{(l)}(\omega)\bar{b}e^{i\vec{\Theta}\cdot(\vec{r}+\overrightarrow{a_1}-\overrightarrow{a_2})} \tag{4.62}$$

$$\overline{\delta F}^{err,(l+1)}_{I+1/2,J+3/2}(\vec{r},\omega) = \bar{\bar{A}}^{acc,(l)}(\omega)\bar{\bar{\vartheta}}^{(l)}(\omega)\bar{b}e^{i\vec{\Theta}\cdot(\vec{r}+\overrightarrow{a_1}+3\overrightarrow{a_2})} \tag{4.63}$$

$$\overline{\delta F}^{err,(l+1)}_{I+3/2,J+1/2}(\vec{r},\omega) = \bar{\bar{A}}^{acc,(l)}(\omega)\bar{\bar{\vartheta}}^{(l)}(\omega)\bar{b}e^{i\vec{\Theta}\cdot(\vec{r}+3\overrightarrow{a_1}+\overrightarrow{a_2})} \tag{4.64}$$

For the error quantities $\overline{\delta\phi}^{err,(l)}_{I',J'}$ and $\overline{\delta\phi}^{err,(l,M)}_{I',J'}$, the Fourier ansatz are the ones defined in Eqs. (4.31) and (4.37).

Eqs. (4.60) to (4.64), (4.31) and (4.37) are entered in Eq. (4.59). The resulting equation gives a relationship between $\bar{\bar{\vartheta}}^{(l)}$ and $\bar{\bar{\xi}}^{acc,(l,M)}_{2-D}$ and reads as:

$$\bar{\bar{\vartheta}}^{(l)} = \bar{\bar{U}}^{-1}\bar{\bar{\chi}}\,\overline{\overline{\nu\Sigma_{\mathrm{f}}}}\Delta x\Delta y a\left(\bar{\bar{\xi}}^{acc,(l,M)}_{2-D} - \bar{\bar{I}}\right) \tag{4.65}$$

with

$$\bar{\bar{U}} = \left[4\frac{\Delta y}{\Delta x}\bar{\bar{D}}(1-\cos(\Theta_1\Delta x)) + 4\frac{\Delta x}{\Delta y}\bar{\bar{D}}(1-\cos(\Theta_2\Delta y)) + 2\overline{\overline{\Sigma_R}}\Delta x\Delta y - 2\overline{\overline{\Sigma_{sd}}}\Delta x\Delta y\right] \tag{4.66}$$

Eq. (3.34) that updates the scalar neutron noise in the outer iterations and the definitions of $\overline{\delta F}^{err}$ and $\overline{\delta\phi}^{err,acc}$, are used to obtain:

$$\overline{\delta\phi}^{err,acc,(l+1)}_{I,J} = \overline{\delta\phi}^{err,acc,(l,M)}_{I,J} + \frac{1}{4}\sum_{I'=I}^{I+1}\sum_{J'=J}^{J+1}\overline{\delta F}^{err,(l+1)}_{I'-\frac{1}{2},J'-\frac{1}{2}} \tag{4.67}$$

In this equation the Fourier ansatz for the error quantities is introduced and the relationship between $\bar{\bar{A}}^{acc,(l)}$ and $\bar{\bar{A}}^{acc,(l+1)}$ is derived:

$$\bar{\bar{A}}^{acc,(l+1)} = \left[\bar{\bar{\xi}}^{acc,(l,M)}_{2-D} + \frac{a}{2}\bar{\bar{\vartheta}}^{(l)}\right]\bar{\bar{A}}^{acc,(l)} \tag{4.68}$$

Eqs. (4.65) and (4.68) are combined and the spectral radius of the overall DSA scheme can be calculated as:

$$\rho_{DSA}\left(\omega, M, \vec{\Theta}\right) = \max\left\{\mathrm{abs}\left[\mathrm{eig}\left(\bar{\bar{\xi}}^{acc,(l,M)}_{2-D} + \frac{a^2}{2}\bar{\bar{U}}^{-1}\bar{\bar{\chi}}\,\overline{\overline{\nu\Sigma_{\mathrm{f}}}}\Delta x\Delta y\left(\bar{\bar{\xi}}^{acc,(l,M)}_{2-D} - \bar{\bar{I}}\right)\right)\right]\right\} \tag{4.69}$$

where $\bar{\bar{\xi}}^{acc,(l,M)}_{2-D}$ is given by Eq. (4.55). The convergence rate of the DSA scheme can thus be evaluated by taking the maximum of $\rho_{DSA}\left(\omega, M, \vec{\Theta}\right)$ over all error modes.

4.1.3 Convergence rate for 1-D and 2-D calculations

For the current analysis, the generic equation for the theoretical spectral radius can be written as follows:

$$\rho_{generic}\left(\omega, M, \vec{\Theta}\right) = max\left\{abs\left[eig\left(f\left(\bar{\bar{\xi}}^{(l,M)}\right)\right)\right]\right\} \tag{4.70}$$

where $f\left(\bar{\bar{\xi}}^{(l,M)}\right)$ indicates a function of the matrix $\bar{\bar{\xi}}^{(l,M)}$. According to the discussion in Paper I and section 4.1.1, the matrix function $f\left(\bar{\bar{\xi}}^{(l,M)}\right)$ in the case of the one- and two-dimensional unaccelerated schemes, is:

$$f\left(\bar{\bar{\xi}}^{(l,M)}_{un}\right) = \bar{\bar{\xi}}^{(l,M)}_{un} = \left[\bar{\bar{I}} - \left(\bar{\bar{I}} - \bar{\bar{P}}\right)^{-1}\left(\bar{\bar{I}} - \bar{\bar{P}}^{M}\right)\bar{\bar{Q}}\right]^{-1}\left[\bar{\bar{P}}^{M} + \left(\bar{\bar{I}} - \bar{\bar{P}}\right)^{-1}\left(\bar{\bar{I}} - \bar{\bar{P}}^{M}\right)\bar{\bar{R}}\right] \tag{4.71}$$

In the equation above, the matrices $\bar{\bar{P}}$, $\bar{\bar{Q}}$ and $\bar{\bar{R}}$ depend on a matrix denoted as $\bar{\bar{T}}$. For the 1-D problem, the matrix $\bar{\bar{T}}$ is given in Eq. (20) in Paper I, i.e.

$$\bar{\bar{T}}_{1D} = \frac{1}{2}\int_{-1}^{1}\left(i\mu\Theta\overline{\overline{\Sigma_t^{dyn}}}^{-1} + \bar{\bar{I}}\right)^{-1} d\mu \tag{4.72}$$

For the 2-D scheme, $\bar{\bar{T}}$ is obtained from Eq. (4.28).

In the 1-D case, Paper I shows that the maximum spectral radius which is related to the convergence rate of the algorithm, is always associated with the zeroth error mode ($\Theta = 0$). In the 2-D case, the same result is found. In Figure 4.1, the plot on the left provides the spectral radius and its dependence on the error mode $\vec{\Theta}$ for a 2-D unaccelerated problem, where the frequency of the neutron noise source is equal to 1 Hz and the number of inner iterations M is equal to 2. When the zeroth error mode is taken, the matrices $\bar{\bar{T}}$ in Eqs. (4.72) and (4.28) are equal to the identity matrix, and so the expression for the spectral radius and the convergence rate becomes identical for 1-D and 2-D problems.

For the DSA scheme, the same conclusion can be drawn as the maximum spectral radius for the accelerated scheme is also associated with $\vec{\Theta} = 0$; see plot on the right in Figure 4.1. The function $f(\bar{\bar{\xi}}^{(l,M)})$ for calculating the spectral radius in the one-dimensional DSA case is given by Eq. (29) in Paper I and is equal to:

$$f\left(\bar{\bar{\xi}}_{1-D}^{acc,(l,M)}\right) = \bar{\bar{\xi}}_{1-D}^{acc,(l,M)} + \left(\Theta^2\bar{\bar{D}} + \bar{\bar{\Sigma}}_R - \bar{\bar{\Sigma}}_{s,d}\right)^{-1}\bar{\bar{\chi}}\,\overline{\overline{\nu\Sigma_f}}\left(\bar{\bar{\xi}}_{1-D}^{acc,(l,M)} - \bar{\bar{I}}\right) \tag{4.73}$$

The function for the two-dimensional DSA scheme is given in Eq. (4.69). Again, the two functions are identical when the zeroth error mode is taken.

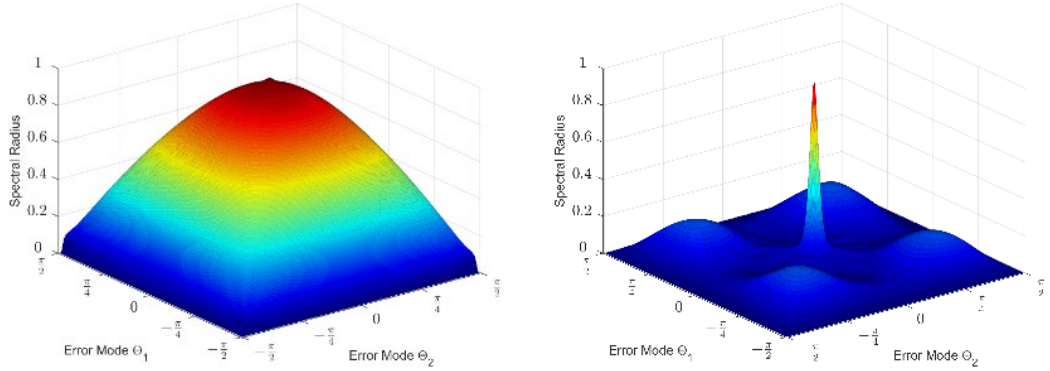

Figure 4.1 Theoretical spectral radius associated with the unaccelerated scheme (left) and the DSA scheme (right), for a neutron noise calculation in a 2-D homogeneous system.

4.1.4 Convergence properties of the unaccelerated and DSA schemes

The convergence properties of the unaccelerated and DSA algorithms are investigated with respect to the number of inner iterations and the frequency of the neutron noise source. In addition, the theoretical and numerical values of the convergence rates are compared. This is part of the verification of the correct implementation of the algorithms. For the purpose, a

problem that consists of a neutron noise source (namely, an absorber of variable strength) in a two-dimensional homogeneous system, is used. The neutron cross sections and the kinetics parameters of the system are taken from [7]. The spatial domain is discretized using a 30×30 square mesh, in which the size of one computational cell is such that $\Delta x = \Delta y = 1\ cm$. For the angular discretization, S_8 level symmetric quadrature set is used. The boundary conditions are reflective, so the system can be considered infinite.

The theoretical predictions of the convergence rate for the unaccelerated and DSA algorithms are respectively calculated with the expressions given in Eqs. (4.29) and (4.69). The numerical convergence rate (denoted as ρ_{num}) is estimated from the simulations as:

$$\rho_{num} = \frac{\left\| \overline{\overline{\delta\phi}}^{(l+1)}(\vec{r},\omega) - \overline{\overline{\delta\phi}}^{(l)}(\vec{r},\omega) \right\|_2}{\left\| \overline{\overline{\delta\phi}}^{(l)}(\vec{r},\omega) - \overline{\overline{\delta\phi}}^{(l-1)}(\vec{r},\omega) \right\|_2} \tag{4.74}$$

where $\| \cdot \|_2$ is the Euclidean norm, and $\overline{\overline{\delta\phi}}^{(l+1)}$, $\overline{\overline{\delta\phi}}^{(l)}$ and $\overline{\overline{\delta\phi}}^{(l-1)}$ are the two-energy group scalar neutron noise column-vectors computed from the solver, respectively, at iterations $(l+1)$, l and $(l-1)$.

Dependence of the convergence rate on the number of inner iterations

Stationary fluctuations of the thermal capture cross-section are introduced in one point of the 2-D homogeneous system. The perturbation has an amplitude equal to unity and a frequency of 1 kHz.

The influence of the number of inner iterations M on the convergence rate is shown in Figure 4.2. The numerical performance of the algorithms is consistent with the theoretical predictions. For the unaccelerated numerical scheme, the spectral radius decreases with more inner iterations performed. On the other hand, the convergence rate of the accelerated scheme is not affected by the number of inner iterations. In fact, when the error-mode is taken to be zero, the matrix $\bar{\bar{T}}$ (Eq. (4.28)) becomes an identity matrix. Then the matrix $\overline{\overline{P^{acc}}}$ (Eq. (4.56)) is zero, which causes the spectral radius in Eq. (4.69) to be independent of M.

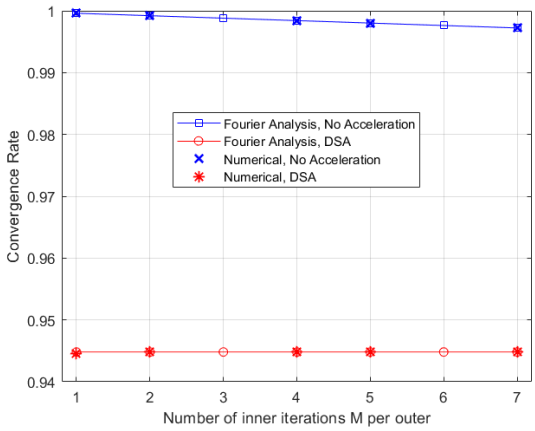

Figure 4.2 Convergence rate as a function of the number of inner iterations M for the accelerated and DSA schemes

Dependence of the convergence rate on the frequency of the neutron noise source

The relationship between convergence rate and frequency of the neutron noise source is explored by varying the frequency of the neutron noise source defined above, i.e. a stationary fluctuation of the thermal capture cross section in one point of the system. The number of inner iterations M is chosen equal to 4. The results are plotted in Figure 4.3 for both the unaccelerated and accelerated schemes. Again, the numerical behavior of the algorithms agrees with the theoretical one. A plateau region is found between ~0.1 Hz and ~100 Hz, where the convergence is rather insensitive to the frequency. Below the frequencies of the plateau region, the spectral radius increases largely with decreasing frequency and the convergence becomes slow. Above the frequencies of the plateau region, the spectral radius decreases with increasing frequency and the trend is more remarkable for the accelerated scheme.

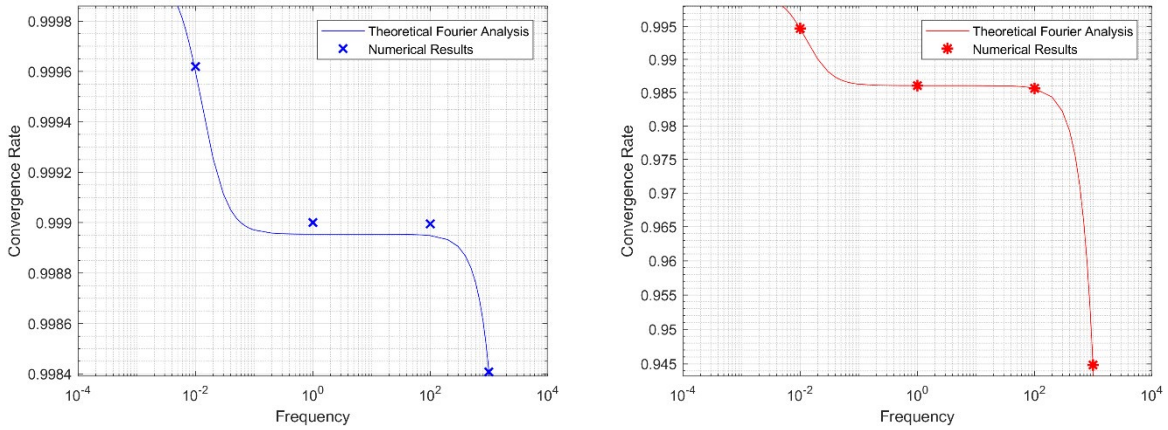

Figure 4.3 Convergence rate as a function of frequency for the unaccelerated scheme (left) and for the DSA scheme (right)

4.2 Neutron noise simulations in heterogeneous systems

The accelerated and unaccelerated solvers are further tested using neutron noise problems based on the two-dimensional C3 and C4V configurations reported in [17].

The C3 and C4V systems consist of a 2×2 assembly arrangement, where two UO_2 assemblies are respectively located North-West and South-East and two MOX assemblies are respectively located North-East and South-West. Each fuel assembly contains 17×17 squares that represents homogenized fuel cells or guide tubes. The C3 test case has reflective boundary condition on all sides of the system while the C4V test case has both reflective and vacuum boundary conditions. The cross-sections used to model the static benchmark problems are given in a two-energy group formalism.

In both the C3 and C4V systems the neutron noise source is assumed to be a stationary fluctuation of the capture cross-section in both energy groups. The source is placed at the fuel cell with position indexes (16,19) which belongs to the North-East MOX fuel assembly. The amplitude of the perturbation is taken to be 5% of the nominal values of the capture cross-section for each group. The frequency of the perturbation is set to 1 Hz. In addition, a

homogeneous β value equal to 0.0049 and a λ value equal to 0.0797 s^{-1} are chosen. The layout of the benchmark problems with the location of the noise source shown in red is given in Figure 4.4.

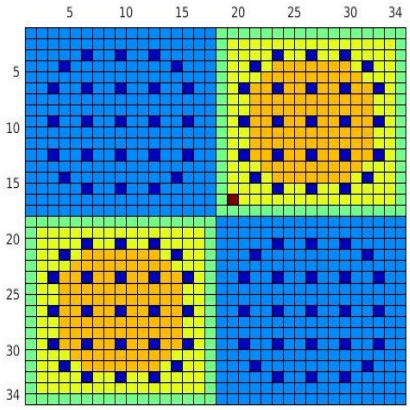

Figure 4.4 System configuration of C3 and C4V benchmark problems with the neutron noise source location labelled in red.

In these calculations, the same 34×34 meshes where each node corresponds to a homogenized fuel cell that has a size of 1.26×1.26 cm, and level-symmetric S_8 quadrature sets are used. In addition, the problems are solved with the unaccelerated and accelerated schemes, using one inner iteration per outer iteration. The convergence criterion for both the static and dynamic module is set to $\varepsilon < 1\mathrm{E} - 7$.

The effective multiplication factor k_{eff} calculated with the unaccelerated and DSA static modules were first compared with the reference values. As reported in Table 4.1, the two algorithms give the same results and the differences with the reference are small, i.e. 52 pcm for the C3 configuration and 62 pcm for the C4V system.

The numerical performances of the unaccelerated and DSA schemes are summarized in Table 4.2. The improvement in the convergence rate is significant when DSA is applied. The number of required iterations is reduced by a factor of at least 13 for the static module and a factor of 20 for the dynamic module.

Table 4.1 Effective multiplication factor k_{eff} calculated by the static module

Problem	Unaccelerated	DSA	Reference
C3	1.01847	1.01847	1.01795
C4V	0.91782	0.91782	0.91720

Table 4.2 Number of outer iterations required for convergence of the unaccelerated and DSA algorithms

Module	System configuration	Unaccelerated	DSA
Static	C3	469	35
	C4V	569	37
Dynamic	C3	30297	1449
	C4V	29991	1436

The dynamic calculations with the unaccelerated and DSA solvers lead to very similar neutron noise results. For each of the two problems, the real part, imaginary part, amplitude and phase of the neutron noise are compared in a point wise manner. The maximum relative difference that is found is less than 0.03%.

The amplitude and phase of the neutron noise of both groups, calculated from the accelerated solver, are plotted in Figures 4.5 and 4.6 for the C3 and C4V problems, respectively. For the two cases, the spatial distribution of the noise amplitude follows the trend of the static fluxes. This outcome is expected since the size of the system is relatively small, and thus the system behaves in a point-kinetic manner. At the location of the perturbation, a local peak is observed in the fast and thermal neutron noise. The phase is close to 180 degrees and slightly decreases when moving away from the location of the neutron noise source. The calculated phase is consistent with the fact that the perturbation is defined in the capture cross-section and an out of phase behavior should result in the response of neutron flux. The decrease of the phase is also expected since it indicates that the response of the neutron flux to the perturbation is a little delayed further away from the source.

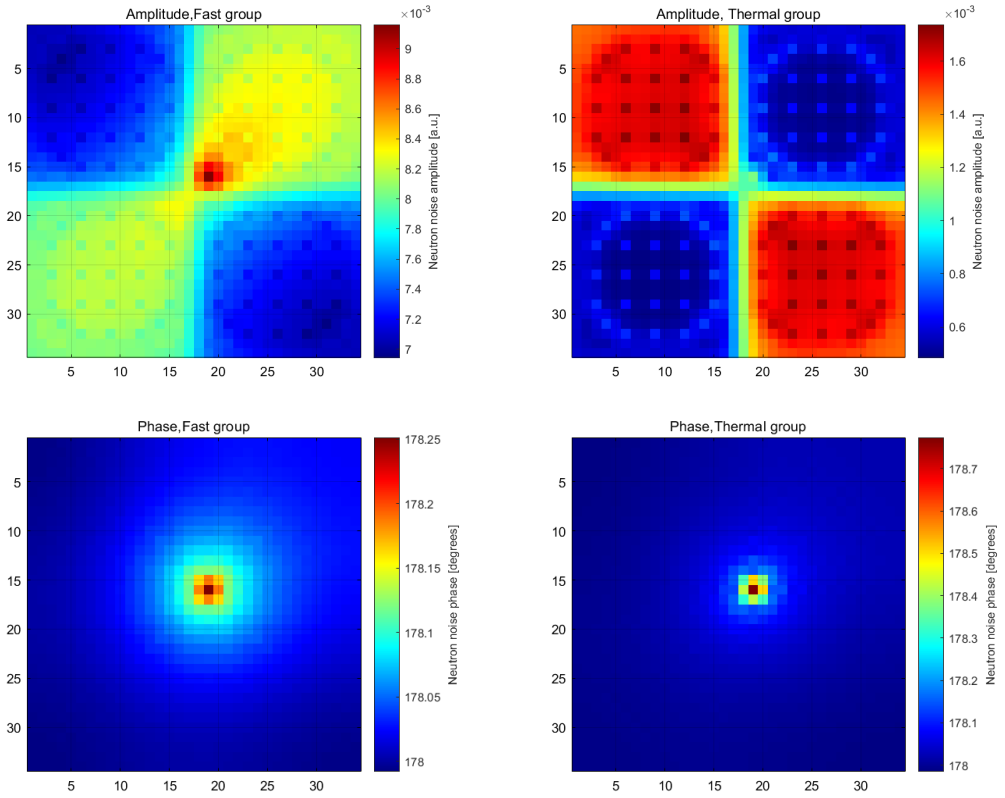

Figure 4.5 Neutron noise obtained from the DSA solver for the C3 case; fast (top-left) and thermal (top-right) amplitude and fast (bottom-left) and thermal (bottom-right) phase

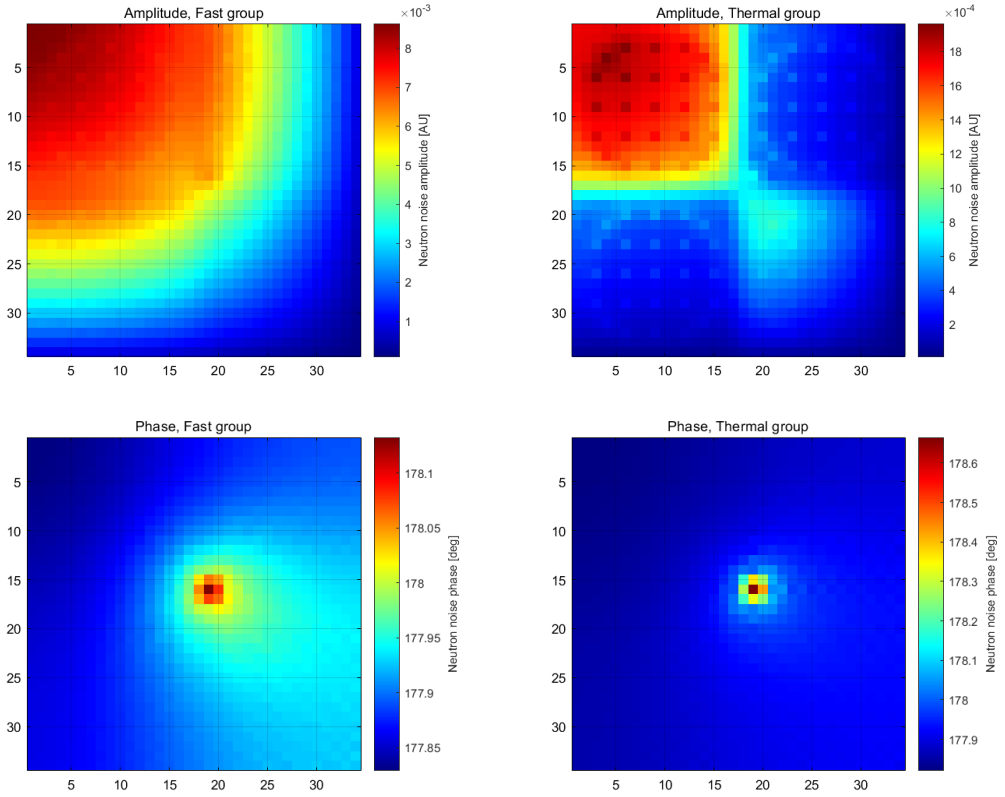

Figure 4.6 Neutron noise obtained from the DSA solver for the C4V case; fast (top-left) and thermal (top-right) amplitude and fast (bottom-left) and thermal (bottom-right) phase

4.3 Comparison with the diffusion-based simulator CORE SIM

The solver is compared to the neutron noise simulator CORE SIM. Both computational tools solve Eqs. (2.6) and (2.8), but the CORE SIM scheme relies on the diffusion approximation.

On one hand, the test contributes to the verification of the solver presented in this work, since CORE SIM has been used to analyse different neutron noise scenarios in the past. On the other hand, the comparison can also provide insights into possible limitations of lower-order methods as the one applied in CORE SIM. For the purpose, the C3 configuration is chosen and a fluctuation of the capture cross section in the fuel cell (16,19) is introduced with the frequency of 1 Hz, as described in the previous section. The complete discussion can be found in Paper II. The results for the two neutron energy groups are similar, so the focus of the section is narrowed to the thermal case in which the discrepancies are wider.

Calculations of both simulators are first performed with different computational spatial grids. In Figure 4.7, the amplitude of the thermal neutron noise predicted by CORE SIM (full blue line with circles) and by the S_N solver (full line with stars) at the location of the perturbation, are plotted with respect to the resolution of the grid. The relative differences are also included (dashed red line). The coarser mesh is the mesh used in the previous section where each node corresponds to the size of each fuel cell/guide tube. Then the mesh is progressively refined from 2×2 to 8×8 equal square nodes per fuel cell/guide tube. As shown in the plot, the results obtained from the meshes with 5×5, 6×6, 7×7 and 8×8 nodes per fuel cell/guide tube are similar and can be considered mesh-independent. In addition, S_8 and S_{16} approximations are used for the angular direction; some 'ray effect' affects the coarser option, even though they are not severe (see details reported in Paper II). Then the mesh with 5×5 nodes per fuel cell/guide tube and the S_8 discretization of the angular variable are selected.

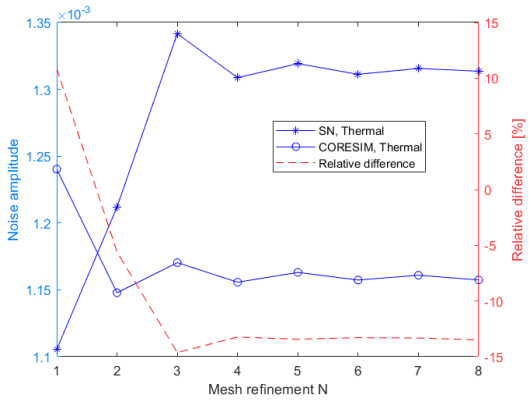

Figure 4.7 Effect of the spatial grid resolution on the amplitude of the thermal neutron noise at the location of the noise source

4.3.1 Static flux and neutron noise calculated with the 2 solvers

The comparison between the static fluxes calculated with the two solvers is shown in the plot on the left in Figure 4.8. The biggest difference is observed in the guide tubes of the MOX fuel

assemblies. The guide tubes introduce abrupt variations of the material properties of the system and these strong heterogeneities can be resolved better with higher-order transport methods than diffusion. The relatively large discrepancies in the guide tubes are also observed in the neutron noise calculations (see plot on the right in Figure 4.8). This is expected because the system under study is small and its response is characterized by a dominant point-kinetic component. Then the spatial distribution of the neutron noise tends to follow the static flux. Additional large differences are found at the location of the neutron noise source and its close surroundings ($\sim -14\%$). For other locations in the system, the differences are quite small (less than 3%). The phase of the neutron noise predicted from both solvers also show negligible differences; a maximum relative difference is found to be less than 0.1%.

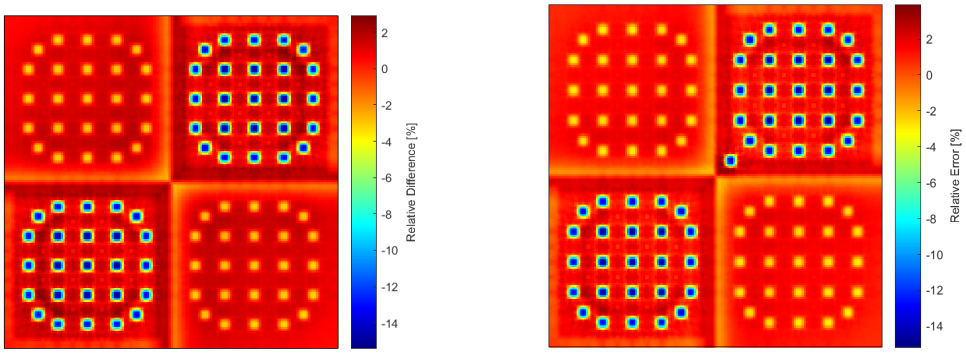

Figure 4.8 Spatial distribution of the relative differences between the two simulators, in the thermal neutron static flux (left) and in the thermal neutron noise (right)

4.3.2 Dependence on the frequency of the neutron noise source

The relative differences between the two solvers are also investigated for other frequencies, within the interval 0.01 Hz and 100 Hz. In Figure 4.9, the results are shown for the central computational node of different fuel cells/guide tubes in the system, viz.: (16,19) where the noise source is placed; (17,18) as representative of fuel cells close to the perturbation; (31,4) as representative of the guide tubes in the MOX fuel assemblies; and (25,10) as a representative of the fuel cells far away from the perturbation. The position indexes used to identify the fuel cells/guide tubes are consistent with Figure 4.4.

The behaviour of the calculated neutron noise amplitude with respect to frequency is consistent with the zero-power reactor transfer function. Therefore, the amplitude decreases as the frequency of the perturbation increases, except in a plateau region at intermediate frequencies where the amplitude is almost constant. This is again explained by the fact that the system is driven by point-kinetics essentially, due to the small size of the system, with the point-kinetic response given by the zero-power reactor transfer function.

The discrepancies between the discrete ordinates solver and CORE SIM are nearly constant in the plateau region, otherwise they may become larger with frequencies. This may be explained by the different performances of higher- and lower-order methods to reproduce the propagation of a disturbance in the system. At the location of the perturbation, the relative differences for

the thermal noise amplitude increase from $\sim -8\%$ to $\sim -24\%$ over the frequency range (see Figure 4.9-a). In the close surroundings of the perturbation, they vary from $\sim 3\%$ at 0.01 Hz up to $\sim 4.5\%$ at 100 Hz (see Figure 4.9-b). Large deviations can be found in the guide tubes because of the strong variation of material properties, so they are rather independent of the frequency. For example, at the guide tube (31,4), the relative differences are about -12% (see Figure 4.9-c). The discrepancies at locations away from the perturbation and from strong variations of material properties are negligible and insensitive to frequency. For one of these locations such as the fuel cell (25,10), the relative differences are around 1.2 – 1.6% (see Figure 4.9-d).

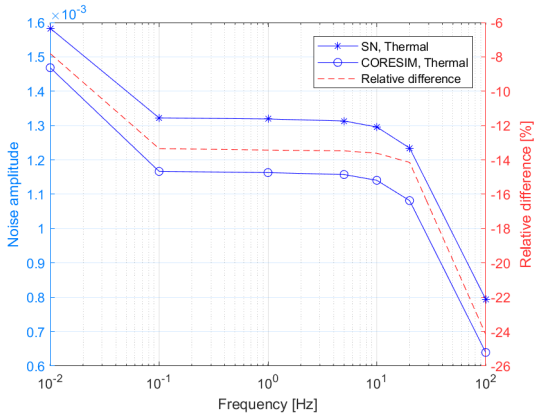

(a) Location of the perturbation (16,19)

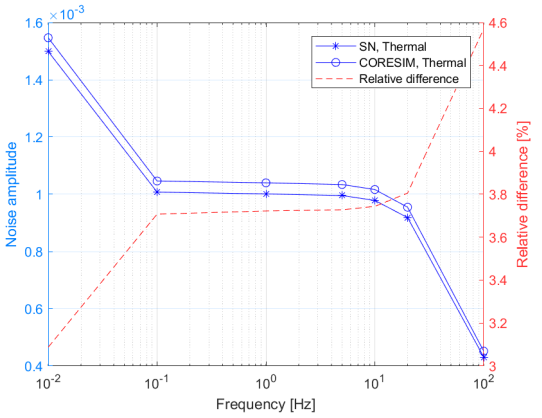

(b) Location (17,18)

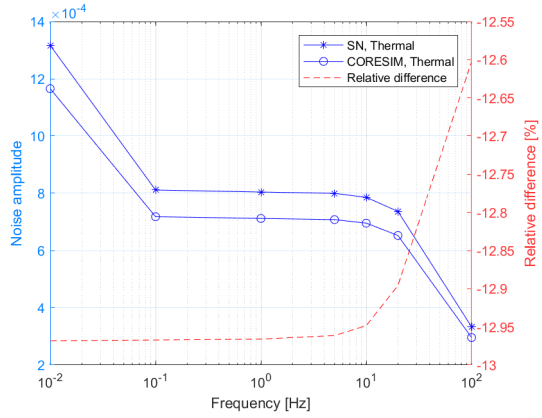

(c) Location (31,4)

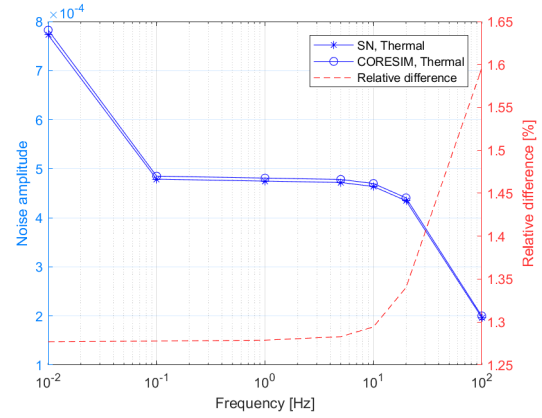

(d) Location (25,10)

Figure 4.9 Amplitude of the thermal neutron noise calculated with the two solvers and relative differences, at various locations in the system

The calculated values of the phase of the thermal neutron noise in the central node of the fuel cell (16,19) and of the guide tube (17,18) are given in Figure 4.10, together with their relative differences. The behaviour with respect to frequency resembles a bell-shaped curve as expected from the zero-power reactor transfer function. The discrepancies between CORE SIM and the discrete ordinates solver are relatively small and constant in the plateau region. For this interval of frequencies, a phase close to 180 degrees is expected because the perturbation of the

macroscopic neutron capture cross-section induces an out-of-phase response of the neutron flux. Outside the plateau region, the relative differences may be somewhat larger. At the location of the perturbation, they are found to be ~ -3% for the thermal neutron noise at the frequency of 0.01 Hz and ~ -3.5% for the thermal neutron noise at the frequency of 100 Hz. When taking other locations, CORE SIM and the discrete ordinates solver provide very similar results. For example, the maximum relative differences are already below 1.2% already in the fuel cell (17,18) which is just next to the perturbed one.

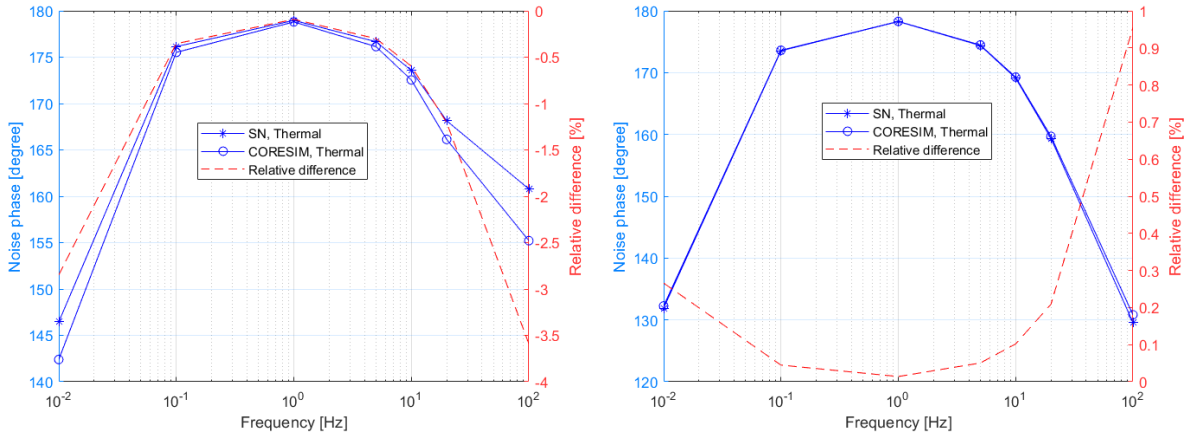

Figure 4.10 Phase of the thermal neutron noise calculated with the two solvers and relative differences, at the location of the neutron noise source (left) and at the location (17,18) (right)

It should nevertheless be emphasized that the good agreement between CORE SIM and the discrete ordinates solver away from the applied perturbation and from material discontinuities is expected to deteriorate when anisotropic scattering is considered. Diffusion-based solvers can be considered as only resolving the isotropic part of the scattering (with a transport correction). Thus, only considering the isotropic part of the scattering in this work for the transport solver is believed to reduce possible discrepancies between diffusion-based and transport-based computations.

Chapter 5

Conclusion and outlook

5.1 Summary

A neutron noise transport simulator based on the 2-D neutron balance equations in the frequency domain, is developed. It consists of a static module that solves the criticality problem and a dynamic module that calculates the neutron noise induced by possible perturbations expressed in terms of stationary fluctuations of the macroscopic cross sections. The equations are discretized according to the discrete ordinates method (with respect to the angular variable) and the diamond finite difference scheme (with respect to the spatial variable). The energy dependence is treated with a two-energy group model. The computational burden of the simulations is reduced by applying the DSA method to both modules.

In order to verify the correct implementation of the algorithm, a study of the convergence and comparisons with the diffusion-based neutron noise simulator CORE SIM are carried out.

The convergence properties of the unaccelerated and accelerated solver are investigated in the case of an absorber of variable strength in an infinite, two-dimensional, homogeneous problem. The maximum analytical spectral radius of the algorithm, which is a measure of the convergence rate, is obtained from the Fourier convergence analysis and agrees with the numerical value estimated from the simulator. The DSA method improves the convergence, but the reduction of the spectral radius at the zeroth error mode is still limited. For both the accelerated and unaccelerated scheme, the convergence rate is slower with decreasing frequency of the perturbation. In addition, a higher number of inner iterations per outer iteration is beneficial for the convergence of the unaccelerated scheme, while it does not influence the accelerated scheme (as expected from the Fourier analysis).

The diffusion synthetic acceleration of the solver is further tested on neutron noise problems derived from the heterogeneous, two-dimensional configurations C3 and C4V. The neutron noise source is defined as the fluctuation of the two-energy group macroscopic capture cross sections associated with one fuel cell of the system. The frequency of the perturbation is 1 Hz. The use of DSA reduces the number of iterations by a factor of 20.

For the comparisons with CORE SIM, the neutron noise problem based on the C3 configuration, with the fluctuation of the neutron capture cross section in one fuel cell, is considered. The results show that the new solver is consistent with CORE SIM, although differences can be found because of the strong material heterogeneities of the system, the local impact of the perturbation, and the frequency of the disturbance. This outcome then suggests that higher-order transport methods may provide an important contribution to more accurate simulations of

neutron noise problems and to the assessment of lower-order transport methods such as the diffusion approximation.

5.2 Outlook

In the continuation of this research several developments are needed.

The DSA method lowers significantly the computational cost of the solver, but the number of iterations required for convergence is still large. The effect deteriorates if the frequency of the perturbation decreases. An alternative is to use the CMFD – Coarse Mesh Finite Difference method. This option has been proven to be an efficient acceleration technique in static and transient transport problems, since the combination of a coarse-mesh problem together with the original fine-mesh, higher-order problem can remove the low-frequency components of the error modes that are the slowest to converge. However, its implementation must be explored carefully because of possible issues with numerical stability.

The solver will be extended in such a manner that simulations of three-dimensional and multi-energy group problems can be performed. For more accurate simulations, the treatment of anisotropic scattering is an important capability that will be included.

Further tests for verification and validation are also planned. The solver under development will be used to simulate numerical problems and neutron noise experiments, that are available from the activities of the CORTEX project [2].

References

[1] I. Pázsit and C. Demazière, "Noise techniques in nuclear systems," *Handbook of Nuclear Engineering*, pp. 1629-1737 (2010).

[2] C. Demazière, P. Vinai, M. Hursin, S. Kollias and J. Herb, "Overview of the CORTEX project", *PHYSOR 2018 - Reactor physics paving the way towards more efficient systems*, Cancun, Mexico, April 22-26 (2018).

[3] CORTEX. *Core Monitoring Techniques and Experimental Validation and Demonstration*. URL: http://cortex-h2020.eu/wp-content/uploads/2019/05/CORTEX-Poster.pdf. (last visited January 24, 2020).

[4] C. Demazière, "CORE SIM: A Multi-purpose Neutronic Tool for Research and Education," *Annals of Nuclear Energy*, **38**(12), pp. 2698-2718 (2011).

[5] M. Bahrami and V. Naser, "SN Transport Method for Neutronic Noise Calculation in Nuclear Reactor Systems: Comparative Study Between Transport Theory and Diffusion," *Annals of Nuclear Energy*, **114**, pp. 236-244 (2018).

[6] A. Rouchon, A. Zoia and R. Sanchez, "A New Monte Carlo Method for Neutron Noise Calculations in the Frequency Domain," *Annals of Nuclear Energy*, **102**, pp. 465-475 (2017).

[7] T. Yamamoto, "Monte Carlo Method with Complex-valued Weights for Frequency Domain Analyses of Neutron Noise," *Annals of Nuclear Energy*, **58**, pp. 72-79 (2013).

[8] C. Demazière, A. Tatidis and P. Vinai, "Monte Carlo-based dynamic calculations of stationary perturbations." Accepted at *PHYSOR 2020 – Transition to a scalable future*, Cambridge, United Kingdom, March 29-April 2, 2020.

[9] E. E. Lewis and W. F. Miller, "Computational methods of neutron transport." (1984)

[10] G. R. Cefus and E. W. Larsen, "Stability analysis of coarse-mesh rebalance," *Nuclear Science and Engineering*, **105**(1), pp. 31-39 (1990).

[11] E. W. Larsen, "Unconditionally stable diffusion-synthetic acceleration methods for the slab geometry discrete ordinates equations. Part I: Theory," *Nuclear Science and Engineering*, **82**(1), 47-63 (1982).

[12] H. G. Joo and J. Y. Cho, (2002). "Dynamic implementation of the equivalence theory in the heterogeneous whole core transport calculation," *PHYSOR 2002 - International Conference on the New Frontiers of Nuclear Technology: Reactor Physics, Safety and High-Performance Computing*, Seoul, Korea, October 7-10 (2002).

[13] M. Bando, T. Yamamoto, Y. Saito and T. Takeda, "Three-dimensional transport calculation method for eigenvalue problems using diffusion synthetic acceleration," *Journal of Nuclear Science and Technology*, **22**(10), pp. 841-850 (1985).

[14] M. Adams and E. Larsen, "Fast Iterative Methods for Discrete-Ordinates Particle Transport Calculations," *Progress in Nuclear Energy*, **40**(1), pp. 3-159 (2002).

[15] A. Zhu, Y. Xu and T. Downar, "Fourier Convergence Analysis of the Infinite Homogenous Multigroup Time-Dependent Boltzmann Transport Equation Using Discrete Ordinates Formulation," *Nuclear Science and Engineering*, **186**(1), pp. 23-36 (2017).

[16] Y. Y. Azmy and E. W. Larsen, "Fourier analysis of the diffusion synthetic acceleration method for weighted diamond-differencing schemes in cartesian geometries," *Nuclear Science and Engineering*, **95**(2), pp. 106-115 (1987).

[17] C. Cavarec, J.F. Perron, D. Verwaerde, and J. West, "Benchmark Calculations of Power Distribution Within Assemblies (No. NEA-NSC-DOC--94-28)," Nuclear Energy Agency (1994).